Metallicity in the Dissipative Hubbard-Holstein Model: Markovian and Non-Markovian Tensor-Network Methods for Open Quantum Many-Body Systems

M. Moroder[1], M. Grundner[1], F. Damanet[2], U. Schollwöck[1] S. Mardazad[1], S. Flannigan[3], T. Köhler[4], S. Paeckel[1]

1 Department of Physics, Arnold Sommerfeld Center for Theoretical Physics (ASC), Munich Center for Quantum Science and Technology (MCQST), Ludwig-Maximilians-Universität München, 80333 München, Germany.
2 Institut de Physique Nucléaire, Atomique et de Spectroscopie, CESAM, University of Liège, B-4000 Liège, Belgium
3 Department of Physics & SUPA, University of Strathclyde, Glasgow G4 0NG, United Kingdom
4 Department of Physics and Astronomy, Uppsala University, Box 516, S-751 20 Uppsala, Sweden

Abstract

The Hubbard-Holstein Hamiltonian describes a prototypical model to study the transport properties of a large class of materials characterized by strong electron-phonon coupling. Even in the one-dimensional case, simulating the quantum dynamics of such a system with high accuracy is very challenging due to the infinite-dimensionality of the phononic Hilbert spaces. The difficulties tend to become even more severe when considering the incoherent coupling of the phonon-system to a practically inevitable environment. For this reason, the effects of dissipation on the metallicity of such systems have not been investigated systematically so far. In this article, we close this gap by combining the non-Markovian hierarchy of pure states method and the Markovian quantum jumps method with the newly introduced projected purified density-matrix renormalization group, creating powerful tensor network methods for dissipative quantum many-body systems. Investigating their numerical properties, we find a significant speedup up to a factor ~ 30 compared to conventional tensor-network techniques. We apply these methods to study quenches of the Hubbard-Holstein model, aiming for an in-depth understanding of the formation, stability, and quasi-particle properties of bipolarons. Our results show that in the metallic phase, dissipation localizes the bipolarons. However, the bipolaronic binding energy remains mainly unaffected, even in the presence of strong dissipation, exhibiting remarkable bipolaron stability. These findings shed new light on the problem of designing real materials exhibiting phonon-mediated high-T_C superconductivity.

Contents

1   Introduction

Since the discovery of high-temperature superconductivity in cuprates [1–4], the quest to identify the underlying pairing mechanism caused an ever-since rapidly increasing theoretical exploration of effective models for strongly-correlated electronic systems [5–9]. While this stimulated the unravelling of unconventional pairing mechanisms [10], the well-known electron-phonon coupling does not seem to be a proper candidate for stabilizing high-temperature superconductivity (at ambient pressure). The conventional argument for this assessment can be illustrated best in one dimension at the example of the Hubbard-Holstein model, where it is established that the electron-phonon interaction generates tightly bound yet heavy electron pairs, dressed by lattice vibrations (bipolarons). The bipolarons' effective mass increases much faster than the corresponding electronic binding energy, rendering a charge-ordered insulating state the energetically more favorable [11–13]. Nevertheless, in the regime of intermediate electron-phonon interactions, the existence of a metallic phase has been established, in which light bipolarons can exist, yet with a much smaller pair-binding energy [14, 15]. Recent theoretical studies considered the effect of anharmonicities on the properties of the metallic phase in the Hubbard-Holstein model, indicating the tendency to stabilize light bipolarons even at larger electron-phonon couplings [16, 17], a crucial requirement for large transition tempera-
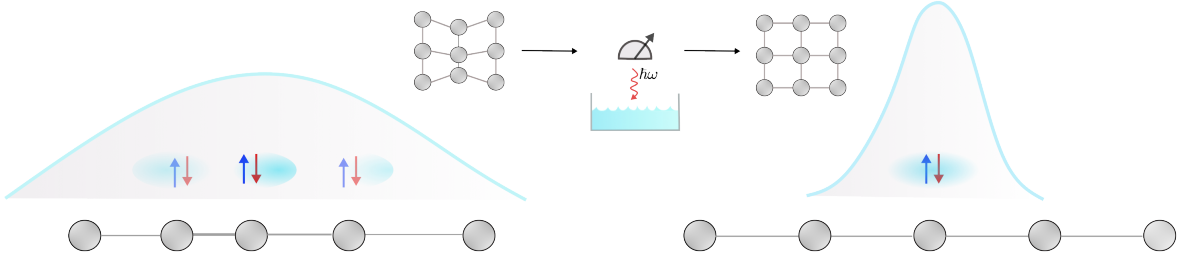
Figure 1: Summary of our main finding: Dissipation tends to localize the bipolarons by means of effective, non-projective measurements. However, in the metallic regime, the bipolaronic binding energy remains mainly unaffected, i.e., bipolarons are stable even for strong dissipation.

tures into a superconducting state. However, the anharmonic contributions to the phononic oscillator potentials have been incorporated in a simplified way, such that the resulting models can be treated semi-analytically. This is mainly due to the extremely high numerical costs for simulating phononic degrees of freedom, whose local Hilbert spaces are, in principle, infinite-dimensional. The computational limitations become even more severe when incorporating more realistic foundations for anharmonicities, such as treating the phononic system as an open quantum system (OQS) or considering dispersive behavior [18, 19]. The past decades have also seen a rapid development of highly efficient numerical tools, enabling simulations of a large number of quantum mechanical degrees of freedom. In particular, the density-matrix renormalization group (DMRG) in its matrix-product state (MPS) formulation [20–23] provides a well-established framework in today's efforts with application ranging from (near-)equilibrium studies of low-dimensional lattice systems [24–31], out-of-equilibrium simulations following global quenches [32–42], impurity solvers for quantum embedding techniques [43–48] or as solver in coupled-cluster techniques to study large molecules [49–54]. Despite its large success on isolated quantum systems, effective numerical schemes to simulate OQSs using MPS are typically applicable only in the Markovian regime [55–68]. Yet, non-Markovian (i.e., spectrally structured) environments are the standard in real materials [69, 70], and it is thus crucial to understand their effects on quantum many-body systems. This becomes even more relevant given the remarkable development of experimental platforms such as ultracold quantum gases [71–75], high-quality electromagnetic cavities [76–81], time-resolved pump-probe experiments on photosynthetic complexes [82], and large arrays of superconducting qubits [83–89]. These platforms make it possible to study the effects of dissipation in cleaner environments but also to investigate the possibility to exploit them as a resource to engineer new phenomena in OQS [90–94]. This work aims to close the gap between the necessity of un-biased descriptions of OQS on the one hand, and numerically efficient lattice representations, operating on the required large local Hilbert spaces on the other hand. For that purpose, we combine a recently introduced mapping of bosonic Hilbert spaces [97, 98] with well-known techniques to describe lattice OQS [93, 94, 99, 100], obtaining powerful, MPS-based tools. We test and benchmark the obtained methods at the example of the dissipative Hubbard-Holstein model in a large parameter space and explore their applicabilities as a function of the electron-phonon coupling and dissipation strength.

Having these tools at hand, we are able to study the effect of realistic phonon-anharmonici-

Lindblad & quantum jumps: Sec. 2.1,
Homodyne detection: App. D
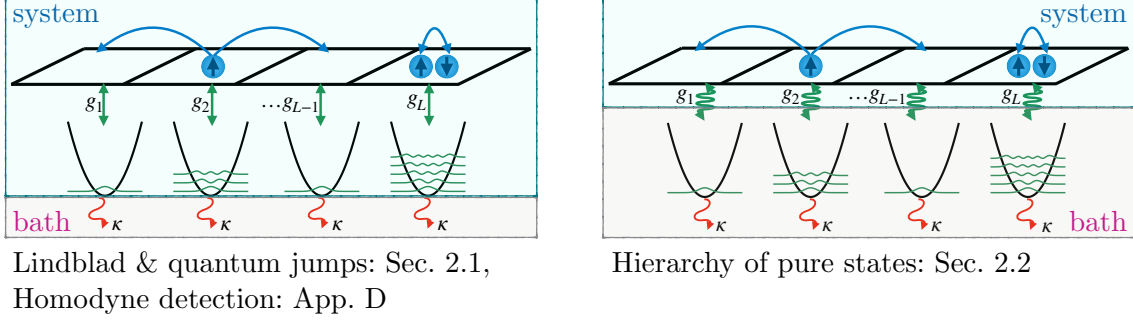

Hierarchy of pure states: Sec. 2.2

Figure 2: Cartoon of two possible system-bath partitioning of electron-phonon systems. Markovian system (left): when considering the electrons and the phonons as the system, the dissipative terms acting on the phonons can be modelled as Markovian. Non-Markovian system (right): if only the electrons are treated as the system, the damped phonon modes constitute a non-Markovian bath. Below both images, a short list of the Markovian and non-Markovian methods analyzed here is given, together with the corresponding section. For the non-Markvian hierarchy of equations of motion (HEOM) method, we refer to [95, 96].

ties on electron-phonon quasi-particles (polarons, bipolarons), originating from the dissipative character of the phonons. Here, our main focus is to answer the question of whether or not dissipation enhances the metallic behavior of (tightly) bound bipolarons. We conduct a systematic analysis of their binding energy and effective mass, whose ratio serves as a measure of their metallicity. Surprisingly, in the strong coupling regime, we find a significant suppression of the metallicity compared to the non-dissipative case, which we interpret as a dissipation-induced measurement, localizing the bipolarons and thereby suppressing transport, as summarized in Fig. 1. However, our calculations also reveal that bipolarons in the metallic regime are unexpectedly stable, even in the presence of strong dissipation.

The article is structured as follows. In Sec. 2 we briefly review the Markovian quantum jumps (QJ) method [100] and the non-Markovian hierarchy of pure states (HOPS) method [99], and introduce their efficient MPS realization, using the recently developed projected purification (PP) mapping. Then, in Sec. 3 we apply HOPS and QJ to study the effect of dissipation on the bipolarons in the Hubbard-Holstein model, and in Sec. 4 we summarize our findings. In App. C, a systematic comparison between QJ and HOPS can be found.

2 Methods

Dissipative electron-phonon systems can be described in two different ways, depending on how they are decompose into a "system" and an "environment". Thus, in this section, we present both a Markovian (system = electrons + phonons) and a non-Markovian (system = electrons only) open system method. These methods can be combined with MPS techniques in order to be able to treat many-body systems. The electron-phonon Hamiltonian we considered takes the form:

$$\hat{H}_{\text{tot}} = \overbrace{\underbrace{\hat{H}_{\text{f}}}_{\text{non-Markovian sys.}} + \hat{H}_{\text{b}} + \hat{H}_{\text{int}}}^{\text{Markovian sys.}} = \hat{H}_{\text{f}} + \sum_j \omega_j \hat{a}_j^\dagger \hat{a}_j + \sum_j g_j \big(\hat{L}_j \hat{a}_j^\dagger + \hat{L}_j^\dagger \hat{a}_j \big) , \qquad (1)$$

where $\hat{H}_f$ is an arbitrary Hamiltonian acting on the fermionic degrees of freedom, $\hat{H}_b$ describes a collection of harmonic oscillators representing the phonons, and $\hat{L}$ is an operator acting on the fermions. The index j labels the lattice sites and the parameters ω_j and g_j are the vibration frequencies of the harmonic oscillators and the electron-phonon coupling constants, respectively. In addition to the unitary dynamics described by Eq. (1), we consider dissipation of the form of phonon losses so that the time evolution of the "electron+phonon" density matrix is described by the Lindblad master equation [101]:

$$\partial_t \hat{\rho} = -i[\hat{H}_{\text{tot}}, \hat{\rho}] + \sum_l \hat{D}_l \hat{\rho} \hat{D}_l^\dagger - \frac{1}{2}\{\hat{D}_l^\dagger \hat{D}_l, \hat{\rho}\} \,, \tag{2}$$

where $\hat{D}_j = \sqrt{\kappa}\hat{a}_j$ are the corresponding Lindblad operators acting on each phononic lattice site.

2.1 Quantum jumps

In the left panel of Fig. 2 we show a system decomposition where both the electrons and the phonons are part of the physical system, and dissipation acts on the phonons only. This representation can be modeled as Markovian via the master equation Eq. (2), which can be rewritten as an evolution for pure states with a stochastic process so that averaging over its samples gives the correct expectation values for the observables. From a numerical point of view, this is highly beneficial since for each random process one only has to store the $\mathcal{O}(\sqrt{N_\rho})$ complex coefficients, with N_ρ being the number of entries of the density matrix of the electron-phonon system. A typical so-called pure state unravelling of the Lindblad equation Eq. (2) is given by the QJ method (we discuss a different unravelling, the homodyne detection method in App. D). Working with pure states, a stochastic process $\mathcal{Q}$ is introduced so that the density matrix, time-evolved by the Lindblad equation, is obtained from averaging over many realizations of the stochastic process:

$$\mathcal{E}[|\Psi(t)\rangle_q \langle\Psi(t)|_q] = \hat{\rho}(t) \,, \tag{3}$$

where $q \in \mathcal{Q}$ is a collection of pseudo-random numbers identifying a so-called trajectory. Here, every single step q in a trajectory $\mathcal{Q}$ is specified by (i) deciding if a dissipative event (quantum jump) has to occur and (ii) choosing the lattice site where the jump happens. Thereby, instead of constructing the density matrix one computes the expectation values of an observable $\hat{O}$ for every trajectory and averages them according to:

$$\langle\hat{O}\rangle(t) = \mathcal{E}[\langle\Psi(t)|_q \hat{O} |\Psi(t)\rangle_q] \,. \tag{4}$$

In App. A we provide a detailed derivation of the QJ method together with a sketch of the algorithm.

2.2 Hierarchy of pure states

Another bipartition of Eq. (1) is possible by treating the electrons as system only, wrapping the phononic system into a non-Markovian bath, as shown in the right panel of Fig. 2. Tracing out the phonons in Eq. (2) makes it possible to derive a non-Markovian stochastic Schrödinger equation [102] for the fermionic degrees of freedom only $|\psi(t)\rangle$:

$$\partial_t |\psi(t)\rangle = -i\hat{H}_f |\psi(t)\rangle + g\sum_j \hat{L}_j z_j^*(t) |\psi(t)\rangle - g\sum_j \hat{L}_j^\dagger \int_0^t \mathrm{d}s\, \alpha_j^*(t-s)\frac{\delta |\psi(t)\rangle}{\delta z_j^*(s)}. \tag{5}$$

Here $\alpha_j(t)$ represents the environment correlation function, which on site j and at zero temperature is given by the Fourier-transform of the spectral density $J_j(\omega)$. Furthermore, $z_j(t)$ denotes a colored noise that satisfies $\mathcal{E}\left[z_j(t)z_{j'}^*(t')\right] = \alpha(t-t')\delta_{j,j'}$, while the term $\delta/\delta z_j^*(s)$ represents the functional derivative with respect to z^*. The observables for the electronic system are then obtained by averaging the dynamics of Eq. (5) over many trajectories. In practical calculations, solving Eq. (5) is exceptionally challenging because of the last term of the right-hand side, which is non-local in time [103]. This problem can be solved efficiently by the HOPS method [93, 99], where one defines:

$$|\psi^{(1,j)}(t)\rangle = D_j(t)\,|\psi(t)\rangle \equiv \int_0^t \mathrm{d}s\,\alpha_j^*(t-s)\frac{\delta\,|\psi(t)\rangle}{\delta z_j^*(s)} \tag{6}$$

which is labeled *first auxiliary state* relative to site j. One then introduces the *k-th auxiliary state* in a recursive manner:

$$|\psi^{(k,j)}(t)\rangle = [D_j(t)]^k\,|\psi(t)\rangle\;, \tag{7}$$

and defines a state on the combined fermionic and bosonic Hilbert space as:

$$|\Psi(t)\rangle = \sum_{\mathbf{k}} C_{\mathbf{k}}(t)\,|\psi^{(\mathbf{k})}(t)\rangle \otimes |\mathbf{k}\rangle^{\mathrm{bos}}\;, \tag{8}$$

where $|\mathbf{k}\rangle^{\mathrm{bos}} \equiv \otimes_j |k\rangle_j^{\mathrm{bos}}$ labels an effective bosonic mode corresponding to the k-th auxiliary state and $C_{\mathbf{k}}(t)$ is a time-dependent coefficient. The hierarchy then takes the form of a simple Schrödinger equation for the state on the combined fermionic and bosonic Hilbert space (see App. B for a detailed description and the full representation of the effective Hamiltonian and a sketch of the HOPS algorithm). Being a pure state method, HOPS [104] is more suited for many-body systems than its density matrix formulation, the so-called HEOM method [95, 96]. Moreover, time-evolving density matrices with MPS methods is non-trivial since one needs to guarantee the positivity of ρ at all times [105]. In the next section, we present how the open systems methods described above can be hybridized with many-body approaches to tackle the non-Markovian dynamics of many-body systems.

2.3   Matrix-product states and Projected purification

Matrix-product states [106–108], also known as tensor trains, provide well-established numerical representations for 1D quantum many-body systems. There are efficient MPS algorithms available for both ground state [22, 23, 109] and time dependent [40] problems. Here, we provide a very short introduction to MPS and projected purified DMRG (PP-DMRG) [97, 98], focussing on the relevant technical aspects to combine them with QJ [100] and HOPS [93, 99, 103]. Importantly, exploiting the PP mapping is required to treat the large local bosonic Hilbert spaces efficiently and thus rendering the discussed OQS-techniques suitable for MPS algorithms.

For any pure state with L sites and a finite number of local degrees of freedom $\sigma_1, \sigma_2, ..., \sigma_L$ ($\sigma_i = 1, 2, ..., d_i$ with local dimensions d_i) the coefficient tensor $c_{\sigma_1,\sigma_2,...,\sigma_L}$ can be reshaped as

$$|\Psi\rangle = \sum_{\sigma_1,...,\sigma_L} c_{\sigma_1\cdots\sigma_L}\,|\sigma_1\cdots\sigma_L\rangle \to |\Psi\rangle_{\mathrm{MPS}} = \sum_{\substack{\sigma_1,...,\sigma_L \\ m_0,...,m_L}} M_{1;m_0,m_1}^{\sigma_1}\cdots M_{L;m_{L-1},m_L}^{\sigma_L}\,|\sigma_1\cdots\sigma_L\rangle\;,$$
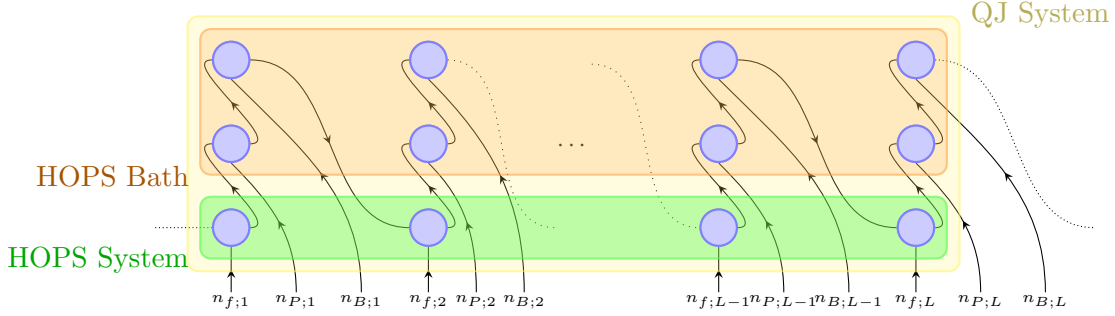
$$\tag{9}$$

Figure 3: MPS representation in an enlarged Hilbert space with each physical site consisting of a physical fermionic, a physical bosonic, and a bosonic bath site. Adapted from [97].

where $\{M^{\sigma_i}_{i;m_{i-1},m_i}\}$ are $m_{i-1} \times m_i$ rectangular matrices. This representation has two main advantages: it allows for optimal and physically motivated compression of the state via singular-value decompositions (SVDs) and decomposes the coefficient tensor into local objects, which, moreover, can be related to the system-environment picture of the original DMRG [20, 21].

MPSs and matrix-product operators (MPOs), which follow the same structure, are often represented graphically in terms of tensor network diagrams. Therein, geometric shapes represent the rank-3 or rank-4 tensors. It is essential to note that the dimensions of the MPS tensors on some site j, called bond dimensions m_j, typically grow exponentially with the entanglement when bipartitioning the system at the sites $j - 1, j$. When it comes to time-evolution methods, time-dependent variational principle (TDVP) [110, 111] is a well-established technique, which is based on the Dirac-Frenkel variational principle and consists of subsequently updating a small number (typically one or two) of site-tensors [40]. One must bear in mind, however, that in its original formulation, this method is particularly prone to cause significant errors when used for time-evolving a product state with a large local Hilbert space dimension [40]. Clearly, MPO-based techniques, such as the time-evolving block decimation (TEBD) [108] or the $W^{\text{I,II}}$ [112], can overcome this limitation, but are also suffering from systematic Trotter errors [113]. However, we found it to be sufficient to time-evolve the state with the slower but more accurate global Krylov method [40] up to the point where the bond dimension is as large as the local Hilbert space dimension and then to switch to TDVP.

The description of bosonic degrees of freedom has posed substantial challenges to MPS methods because of their infinite-dimensional Hilbert spaces. Much work has been devoted to an accurate and efficient truncation of bosonic Hilbert spaces, resulting in successful techniques such as the pseudo site (PS) method [24] and the local-basis optimization (LBO) method [19, 114–117]. In this context, a newly-introduced MPS method is the so-called projected purification [97]. For the class of Hamiltonians described by Eq. (1), the electron-phonon interaction term $\hat{H}_{\text{int}}$ does not conserve the number of phonons. The breaking of the associated $U(1)$ symmetry prevents the site tensors of the MPS from having a block-diagonal structure, resulting in a significant slow-down of matrix operations [118]. For a thorough presentation of the method, we refer to Refs. [97]. The main idea of the PP method is to restore the $U(1)$ symmetry artificially by doubling the bosonic Hilbert space, precisely as one does for the thermal purification method [105] (see Fig. 3), and to modify the bosonic creation
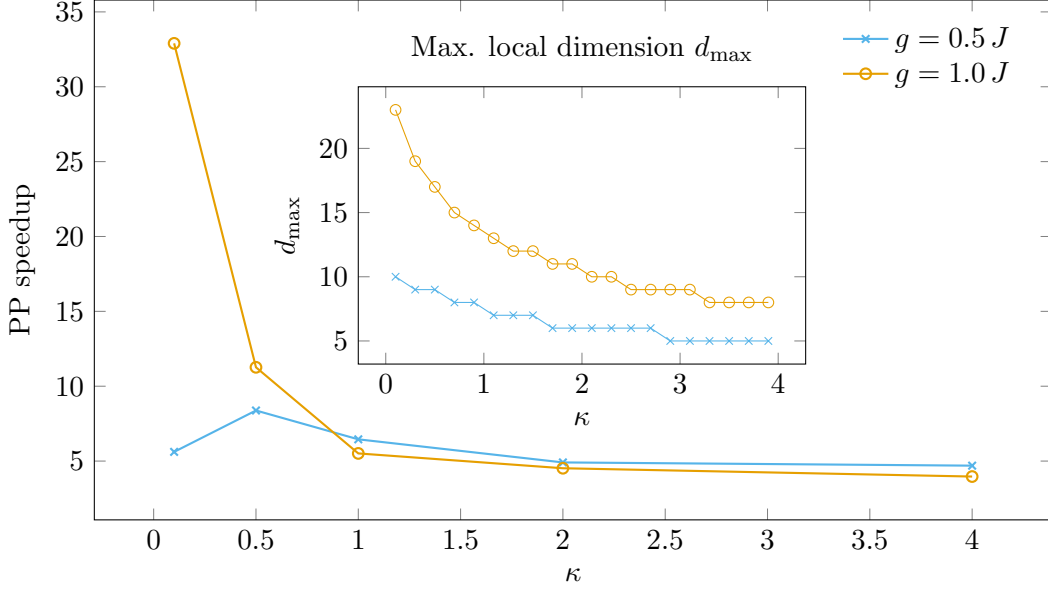
Figure 4: PP speedup for intermediate (blue) and strong (orange) electron-phonon coupling as a function of the dissipation strengths. The speedup factor is significant for large electron-phonon couplings and small dissipation strength, corresponding to a large bosonic local Hilbert space dimension as indicated in the inset. The time evolutions were performed with the QJ method for systems with $L = 20$ sites for a single trajectory. All other parameters were the same as those described in Fig. 15.

and annihilation operators as follows:

$$
\begin{aligned}
\hat{a}_j^\dagger &\to \hat{a}_{P;j}^\dagger \otimes \hat{b}_{B;j} \\
\hat{a}_j &\to \hat{a}_{P;j} \otimes \hat{b}_{B;j}^\dagger \,,
\end{aligned}
\tag{10}
$$

where $\hat{b}_{B;j}$, $\hat{b}_{B;j}^\dagger$ are the bare operators defined in Eq. (33) of App. B. Accompanied by this transformation, a local gauge condition on the allowed states is imposed, i.e., on each pair of physical and bath sites, the sum of the number of physical particles n_P and bath particles n_B has to be conserved $n_P + n_B = n_{\mathrm{ph,max}} - 1$, where $n_{\mathrm{ph,max}}$ is the maximal phononic local Hilbert space dimension. The second key ingredient of the PP method consists in adopting a truncation method for the local Hilbert space dimension of the phononic sites that is analogous to the one exploited by MPS algorithms for truncating the bond dimension. Thereby, imposing a discarded weight δ, defined as the maximally allowed leakage of spectral weight for density matrices belonging to any lattice bipartition, determines a truncation in both the physical dimensions and the bond dimensions. Thus, if the diagonal elements of the phononic reduced density matrices decay fast enough, truncations can reduce the actually used local dimensions: $d_{\mathrm{max}} \le n_{\mathrm{ph,max}}$.

From a more general point of view, it is the decay of the single-site reduced density-matrix (1RDM) diagonal elements ρ_{σ_j,σ_j} that controls the possible speed up generated by the PP mapping. Therefore, while large local dimensions are doable within PP-DMRG, in practice, one has to check for converged diagonal elements of the 1RDM and, if required, increase the maximally allowed local dimension to keep the truncation error δ at an acceptable level.

In App. C we present a detailed benchmark and convergence analysis of the PP-enhanced HOPS and QJ methods for the dissipative Hubbard-Holstein model. Most importantly, both methods are numerically stable and well-controlled in different physical situations, rendering a combination of both an ideal toolset for studying OQS dynamics. While QJ allows for an efficient simulation of weak-and intermediate-dissipation, HOPS reveals its strengths when considering the limit of intermediate to strong dissipation. However, both methods benefit significantly when combined with PP. In Fig. 4 we illustrate the speedup provided by adopting the PP mapping for a system of $L = 20$ lattice sites and one trajectory (note that larger system sizes were out of reach for the reference calculations). We find that the runtime is significantly reduced when using the PP mapping for all analyzed parameters. In particular, we observe a substantial speed-up of a factor of ~ 30 for small dissipation and strong electron-phonon coupling, i.e., for large local Hilbert space dimensions > 20, while it is less significant for medium and strong dissipation (factor ~ 5). Note that the reduced speedup in the strongly dissipating regime is not severe for the overall runtime. This can be attributed to the fact that strong dissipation naturally reduces the correlations in the system and thus the bond dimension, too (c.f., Fig. 17 in App. C). Therefore, combining QJ with PP allows for the numerically efficient application of QJ in exactly that parameter regime, where QJ was also found to be the method of choice.

3   Metallicity in the dissipative Hubbard-Holstein model

The Hubbard-Holstein Hamiltonian describes spinful fermions coupled to Einstein phonons [119]. We consider the one-dimensional case of the form of Eq. (1) that reads:

$$\hat{H}_{\text{HH}} = -J \sum_{j=1}^{L} \sum_{\sigma=\uparrow,\downarrow} \left(\hat{c}_{j,\sigma}^{\dagger} \hat{c}_{j+1,\sigma} + \text{h.c.} \right) + U \sum_{j=1}^{L} \hat{n}_{j,\uparrow} \hat{n}_{j,\downarrow} + \omega \sum_{j=1}^{L} \hat{a}_{j}^{\dagger} \hat{a}_{j} + g \sum_{j=1}^{L} \left(\hat{a}_{j} + \hat{a}_{j}^{\dagger} \right) \hat{n}_{j} . \quad (11)$$

Here, U denotes the onsite Hubbard-interaction while g measures the electron-phonon coupling, and the phonon frequency is given by ω. In the following, we fix J as the unit of energy and J^{-1} as the unit of time. Despite its conceptional simplicity, Eq. (11) provides a minimal model for the complex interplay between lattice vibration and electronic degrees of freedom in the strong coupling regime. Such a physical situation occurs, for instance, in Alkali-doped C_{60} fullerene molecules [120, 121], a class of unconventional superconductors that recently has been investigated for optically induced superconductivity [122–124]. However, understanding in particular the regime of competing (spinless) fermion-phonon and onsite Hubbard-interaction remains a challenging numerical task even in equilibrium, with lots of numerical effort conducted in the past decade [11, 16, 114, 125–131]. We aim to push the limit towards complete microscopic modeling of the out-of equilibrium dynamics, incorporating the effect of dissipation on a strongly-correlated quantum many-body system with up to $L = 40$ lattice sites. We note that the dissipative Hubbard-Holstein model considered here can be derived from a more general perspective, where the electronic degrees of freedom are coupled to a global bosonic environment (see App. E). We emphasize that in contrast to previous works, we made no strong assumptions about the phonons to render it more tractable [16, 17].

The phase diagram of the Hubbard-Holstein model at half-filling sketched in Fig. 5a has been investigated comprehensively, and in the regime of large phonon frequencies, the picture of three different phases has been established [11, 125, 132–136]. In the limit of vanishing
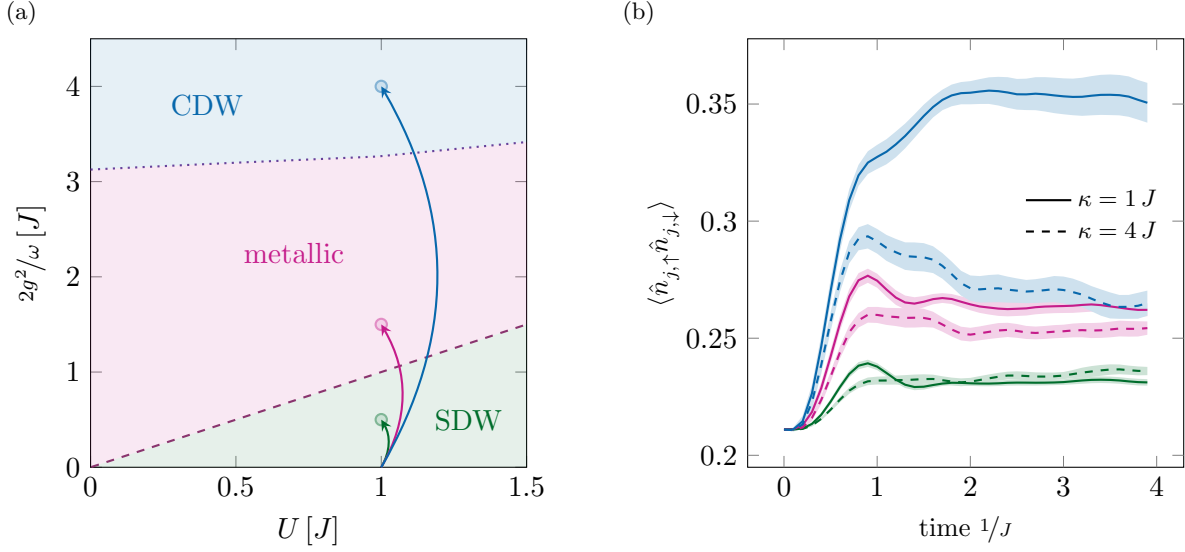
Figure 5: (a) phase diagram of the Hubbard-Holstein model at a constant phonon oscillation frequency $\omega = 2\,J$ adapted from Ref. [11]. The colored arrows indicate quenches from the Hubbard ground state at $U = J$ into the SDW, the metallic and the CDW phase. (b) double occupancy dynamics after global quenches from the Hubbard ground state. They were performed with HOPS at intermediate dissipation $\kappa = J$ (solid line) and strong dissipation $\kappa = 4\,J$ (dashed line). The double occupancy dynamics in the electron systems depend more strongly on the phonon loss rate for large electron-phonon coupling g.

electron-phonon coupling $g/U \to 0$, a correlated spin-density wave (SDW) phase exists, reminiscent of a Hubbard Mott phase. In the opposite limit $g/U \to \infty$, strong phonon fluctuations drive the system into a Peierls state, usually referred to as charge-density wave (CDW) phase. This limit is understood most easily when transforming the Hubbard-Holstein model into a polaronic description through a Lang-Firsov transformation [137]. Then, the Hubbard on-site interaction is renormalized by the phonons as $U \to U - \frac{2g^2}{\omega}$ and for sufficiently large electron-phonon couplings, a dominant attractive interaction between the polarons features a spontaneous breaking of the system's translational symmetry. For intermediate couplings $U \sim \frac{2g^2}{\omega}$, the competition between attractive phonon-mediated polaron-polaron and repulsive electron-electron interactions drive the system towards a metallic Luther-Emery phase [135]. There has been a vivid debate about whether this metallic regime may also realize superconductivity, with today's assessment being that superconducting correlations are always subdominant, compared to charge-correlations [11, 135]. However, when incorporating gaussian or quartic anharmonicities in the phonon potentials, a strengthening of the metallic behavior has been observed and the question of whether anharmonic phonons may even drive the Hubbard-Holstein model into a superconducting state arises [16, 138, 139]. Here, we study the effect of a realistic source of anharmonicities, namely a dissipative coupling of the phonons to an environment.

Dissipation and double occupancy. Previously, the effect of dissipation in the Hubbard-Holstein model has been investigated using HOPS, reporting an enhancement of supercon-

ducting correlations following a quench from a Neel state [93]. We connect to these findings and evaluate the dynamics of the double occupancy $\langle \hat{n}_{j,\uparrow} \hat{n}_{j,\downarrow} \rangle$. As the initial state, we choose the ground state of the Hubbard model ($g = 0$, $\kappa = 0$) at $U = J$, and perform a quench to a point in the SDW phase ($2g^2/\omega = 0.5\,J$), one in the metallic phase ($2g^2/\omega = 1.5\,J$), and one in the CDW phase ($2g^2/\omega = 4\,J$). As a method, we use HOPS, which is particularly tailored for quenching in both κ and g. In Fig. 5b, we show the dynamics of the double occupancy on the central site of a 20-electron system for intermediate ($\kappa = J$) and strong dissipation ($\kappa = 4\,J$). Quenching into the SDW regime of the Hubbard-Holstein phase diagram (green curve), we find only a weak dependency on the dissipation strength. This is consistent with dominant spin-spin correlations in the SDW phase, which are relatively insensitive to the phonon occupations. On the other hand, quenching into the CDW regime of the Hubbard-Holstein phase diagram (blue curve), there is a strong dependency on the dissipation. This can be understood by noting that strong phonon fluctuations drive charge correlations and the formation of double occupations in the Peierls phase. However, increasing the dissipation strength allows the phonons to escape the system, weakening charge correlations. Surprisingly, the quenches into the metallic regime (purple curve) resemble the behavior found in the SDW quenches. The weak dependency on the dissipation strength indicates a strong suppression of charge correlations, already for moderate dissipation, an observation that counteracts the reported observation of enhanced metallicity driven by gaussian or quartic phonon anharmonicities [16, 138, 139]. On the other hand, these findings are still consistent with enhanced superconducting correlations [93].

Polarons and bipolarons. In order to disentangle the roles of g and κ and study the impact of dissipation on quasi-particle formation and their metallicity, we investigate further global quenches from the ground state of the Hubbard-Holstein Hamiltonian at finite g, switching on dissipation. For that purpose, we decompose the electronic annihilation (creation) operators into strictly single- and two-particle operators

$$\hat{c}_{j,\sigma} = \hat{s}_{j,\sigma} + \text{sgn}(\sigma)\hat{s}_{j,\bar{\sigma}}^\dagger \hat{d}_j, \tag{12}$$

where $\hat{s}_{j,\sigma} = \hat{c}_{j,\sigma}(1-\hat{n}_{j,\bar{\sigma}})$ and $\hat{d}_j = \hat{c}_{j,\downarrow}\hat{c}_{j,\uparrow}$. Upon applying a Lang-Firsov transformation [137], the Hubbard-Holstein Hamiltonian acquires the form

$$\hat{H}_{\text{LF}} = -J\sum_{j,\sigma}\left(\hat{D}_j^\dagger\left(\frac{g}{\omega}\right)\hat{c}_{j,\sigma}^\dagger\hat{c}_{j+1,\sigma}\hat{D}_{j+1}\left(\frac{g}{\omega}\right) + \text{h.c.}\right) + U_{\text{eff}}\sum_j \hat{n}_{j,\uparrow}\hat{n}_{j,\downarrow} + \omega\sum_j \hat{a}_j^\dagger\hat{a}_j$$

$$= -J\sum_j\left(\hat{T}_{j,j+1}^{bp} + \sum_\sigma \hat{T}_{j,j+1,\sigma}^p + \hat{U}_j^{bp}\right) + \omega\sum_j \hat{a}_j^\dagger\hat{a}_j, \tag{13}$$

where $U_{\text{eff}} = \left(U - \frac{2g^2}{\omega}\right)$. We, furthermore, introduced the bipolaron potential energy $\hat{U}_j^{bp} = U_{\text{eff}}\hat{d}_j^\dagger\hat{d}_j$, the displacement operator $\hat{D}_j^\dagger\left(\frac{g}{\omega}\right) = e^{g/\omega(\hat{a}_j^\dagger - \hat{a}_j)}$, and the polaronic and bipolaronic hopping operators, $T_{i,j,\sigma}^p$ and $T_{i,j}^{bp}$, respectively:

$$\hat{T}_{i,j,\sigma}^p = \hat{D}_i^\dagger\left(\frac{g}{\omega}\right)\hat{s}_{i,\sigma}^\dagger\hat{s}_{j,\sigma}\hat{D}_j\left(\frac{g}{\omega}\right) + \text{h.c.}, \tag{14}$$

$$\hat{T}_{i,j}^{bp} = \hat{D}_i^\dagger\left(\frac{g}{\omega}\right)\hat{d}_i^\dagger\left(\sum_\sigma \hat{s}_{i,\sigma}\hat{s}_{j,\sigma}^\dagger\right)\hat{d}_j\hat{D}_j\left(\frac{g}{\omega}\right) + \text{h.c.}. \tag{15}$$
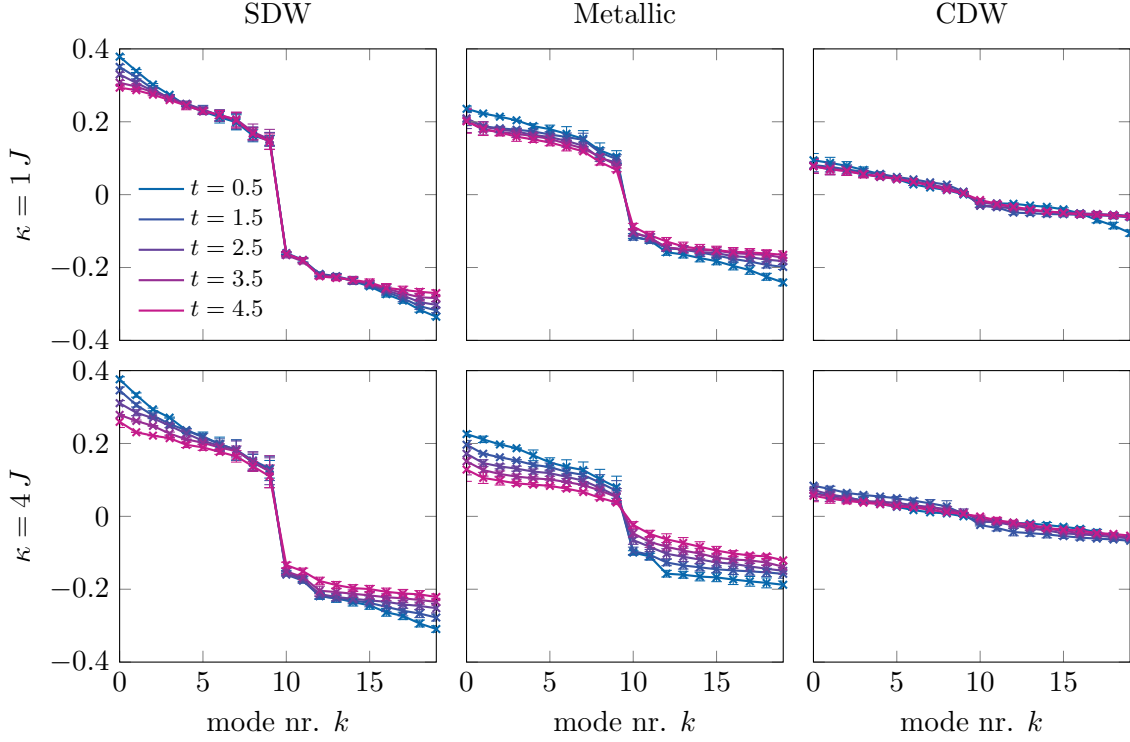
Figure 6: Eigenvalues t_k of bipolaronic hopping matrix $\hat{T}^{bp}_{i,j,\sigma}$ as function of time, after turning on dissipation to $\kappa = 1\,J$ and $\kappa = 4\,J$ in the three different regions of the ground-state phase diagram. In the SDW phase, a large single-particle gap indicates a small bipolaronic effective mass, while the flat band in the CDW phase represents heavy bipolarons. Both phases are basically insensitive to dissipation. In the metallic phase, the gap closing shows that strong dissipation $\kappa = 4$ significantly increases the bipolarons' effective mass. We simulated a system with $L = 20$ sites with QJ, with timestep $dt = 0.01\,J^{-1}$ and computed $|\mathcal{Q}| = 200$ trajectories, using $k_{\max} = 40$ local basis states, a max. bond dimension of $m = 2000$ fixing the discarded weight to $\delta = 10^{-10}$.

Measuring the full hopping matrix $\hat{T}^{bp}_{i,j}$, we can study the kinetic energies t_k of bipolaronic quasi-particles from a diagonalization of $\langle \hat{T}^{bp}_{i,j} \rangle \equiv t^{bp}_{ij}$ where we label the eigenstates by quasi momenta $k_n \equiv \frac{2\pi}{L} n$ with corresponding eigenvalues t_k. As for the quench from the Hubbard ground state, in the following we consider a system with $L = 20$ sites and compute $|\mathcal{Q}| = 200$ trajectories with maximal local dimension $d_{\max} = 40$, maximal bond dimension $m = 2000$, discarded weight $\delta = 10^{-8}$ and timestep $dt = 0.01\,J^{-1}$. We also check, by Fourier transforming the hopping matrix, that assigning the ordered eigenvalue numbers n with quasi momenta is reasonable. From the kinetic energies we determine the maximal quasi-particle velocity v_{eff} by taking the discretized derivative at $k_{\text{eff}} = \pi/2$. Then, in the quasi-particle picture we introduce an estimation for the bipolaronic quasi-particle mass via

$$m_{\text{eff}} = \frac{k_{\text{eff}}}{v_{\text{eff}}} = k_{\text{eff}} \left(\frac{\Delta t_k}{\Delta k} \bigg|_{k_{\text{eff}}} \right)^{-1}. \tag{16}$$
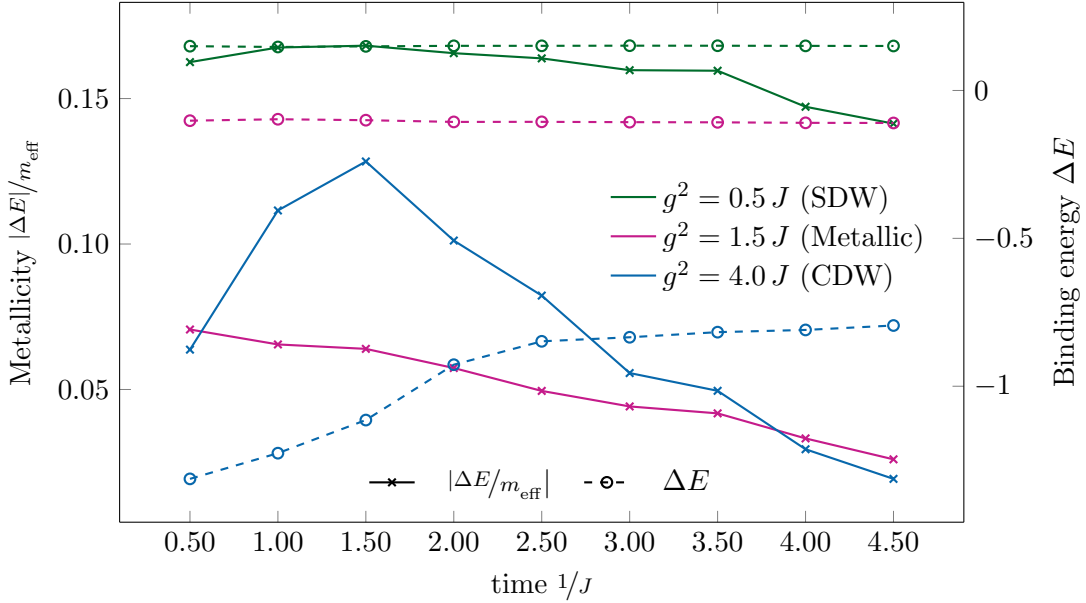
Figure 7: Binding energy (circles) and metallicity (crosses), after the dissipative quenches at $\kappa = 4\,J$ from the three points in the Hubbard-Holstein phase diagram considered in Fig. 6. Analyzing the sign of the binding energy ΔE, we observe the formation of stable bipolarons in the metallic and in the CDW phase, but not in the SDW phase. Most interestingly, in the metallic phase, strong dissipation localizes the bipolarons (the metallicity decreases) without disrupting their stability (ΔE is constant).

If there are stable bipolaronic quasi-particles in the system, then m_eff yields the smallest quasi-particle mass and thereby provides a measure for their metallicity. This interpretation immediately becomes clear, when inspecting the CDW quenches in Fig. 6 (most right column). Here, we observe a nearly flat band over the whole simulation time, indicating the insulating character of the CDW phase that stems from localized bipolarons. In turn, in the SDW phase, a single-particle gap is found, indicating a very small bipolaron effective mass. In the metallic phase, we find the strongest dependency on the dissipation strength. An initially large metallicity is suppressed upon time-evolving for the case of $\kappa = 4\,J$, i.e., the single-particle gap closes, indicating localization of bipolaronic quasi-particles.

Bipolarons' stability and metallicity. In order to determine the stability of bipolaronic quasi-particles, we furthermore calculated the averaged, bipolaronic binding energy [14]. Using Eqs. (14) and (15) this quantity can be written as the difference between the site-averaged bipolaronic and polaronic energies

$$\Delta E = \frac{1}{L} \sum_j \left(\langle \hat{U}_j^{bp} \rangle + \langle \hat{T}_{j,j+1}^{bp} \rangle - \langle \hat{T}_{j,j+1,\uparrow}^{p} \rangle - \langle \hat{T}_{j,j+1,\downarrow}^{p} \rangle \right) \,, \tag{17}$$

where $\Delta E > 0$ indicates that bipolarons are instable and tend to decay into two polarons, whereas $\Delta E < 0$ signals the formation of stable bipolaronic quasi-particles. In Fig. 7, the dashed lines represent the obtained bipolaronic binding energies for the case of strong dissipation. Turning on dissipation in the SDW, ΔE remains constant and positive, i.e., bipolarons
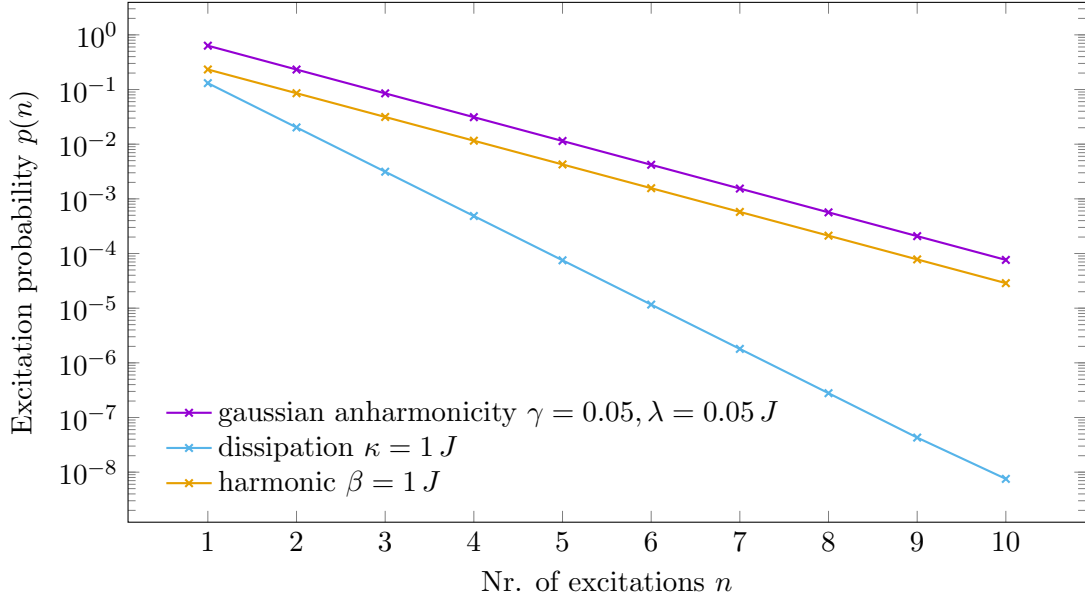
Figure 8: Effect of anharmonicities and dissipation on the excitation probability of bosonic modes. The yellow curve is obtained from evaluating excitation probabilities of a harmonic oscillator $\hat{H}_{\mathrm{HO}}$ at inverse temperature $\beta = 1$. We compare these to the probabilities obtained when adding a gaussian, quadratic anharmonicity $\hat{H}_{\mathrm{HO}} + \lambda e^{-\gamma(\hat{a}^\dagger + \hat{a})^2}$ with $\lambda = 0.05\,J, \gamma = 0.05$ (purple data) and when incorporating dissipation $\kappa = 1\,J$ (blue data). While gaussian anharmonicities reduce the spacing between the energy levels and thus increase the probabilities of populating highly excited states, the effect of dissipation is to leak phonons into the environment, increasing the ground state occupation while higher excitations are suppressed.

are unstable, which is consistent with the insulating character of the antiferromagnetic Hubbard ground state. For the quench in the CDW phase, we find $\Delta E < 0$, which, however, decreases by roughly a factor of two in the scope of the time-evolution on a time scale which is comparable to the phonon frequency ω. Nevertheless, the bipolaronic binding energy is comparably large over the whole time-evolution, indicating stable bipolaronic quasi-particles. In the metallic regime, we also observe $\Delta E < 0$, which surprisingly is nearly time-independent. Thus, in the metallic phase, even in the presence of strong dissipation, phonons that are bound to a bipolaronic quasi-particle do not escape into the environment. Note that these results are in perfect agreement with the time-dependent double occupations shown in Fig. 5b. Indeed, in the metallic regime, the double occupation is nearly independent on the dissipation strength, while the decay of double occupations during the dynamics in the CDW phase at $\kappa = 4\,J$ occurs on the same time scale as the reduction of the bipolaronic binding energy in Fig. 7.

The solid lines in Fig. 7 illustrate the ratio between the absolute value of the binding energy and the effective bipolaron mass. This quantity provides a measure for the bipolaronic metallicity where, for constant binding energies, large ratios correspond to highly mobile bipolarons. The displayed curves provide a compact overview of our analysis, exhibiting the persistent insulating character of both the SDW and CDW phase, also in the presence of dissipation. Moreover, we find a significant decrease in the metallicity in the metallic regime, which is generated by the increased quasi-particle mass of the bipolarons.

Gaussian anharmonicities and dissipation. To connect our results to the reported enhancement of the metallic phase via gaussian and quartic anharmonic modifications of the phononic modes, we compared the effects of dissipation and of the anharmonicities investigated in [16, 138] on the excitation probabilities of a single phonon mode. As a reference distribution, we computed the population of the excited modes by diagonalizing the corresponding Hamiltonian and evaluated the Boltzmann weights at inverse temperature β equal to the oscillator frequency ω. For the dissipative case, it can be shown that the thermal state for a single harmonic oscillator $\hat{\rho}_\beta^{eq} = e^{-\beta\omega\hat{n}}/\mathcal{N}$ is the steady state solution of a Lindblad master equation with Lindblad operators $\hat{D}_1 = e^{-\beta\omega/2}\hat{a}^\dagger$, $\hat{D}_2 = \hat{a}$. Combining them with the Lindblad operator for dissipation $\hat{D}_3 = \sqrt{\kappa}a$ yields the following equation

$$\partial_t\hat{\rho} = -e^{-\beta\omega}\left(\frac{1}{2}\{\hat{a}\hat{a}^\dagger, \hat{\rho}\} - \hat{a}^\dagger\hat{\rho}\hat{a}\right) - (1+\kappa)\left(\frac{1}{2}\{\hat{a}^\dagger\hat{a}, \hat{\rho}\} - \hat{a}\hat{\rho}\hat{a}^\dagger\right) ,\qquad(18)$$

which can be solved numerically. In Fig. 8, we show the excitation probabilities of a harmonic oscillator $\hat{H}_{\mathrm{HO}} = \omega\hat{a}^\dagger\hat{a}$, an anharmonic oscillator with gaussian anharmonicity $\hat{H}_{\mathrm{G}}(\lambda, \gamma) = \hat{H}_{\mathrm{HO}} + \lambda e^{-\gamma(\hat{a}^\dagger+\hat{a})^2}$, and a harmonic oscillator with dissipation Eq. (18). Here, we illustrate the underlying reason for the seemingly contradicting results: dissipation and gaussian anharmonicities have opposite effects on the population of the excited phonon states. While the decay of the excitation probability is reduced by gaussian anharmonicities, it is enhanced when considering dissipation. These observations can be connected to our investigation of metallicity by noting that the binding energy is mainly unaffected by dissipation in the metallic phase. This suggests that the metallicity mainly depends on the mean free path length of the bipolaronic quasi-particles. A recent study has shown that couplings to an environment can be modeled by measurements, suppressing transport via the formation of decoupled clusters [140]. In the limit of very strong dissipation, this is reminiscent of the quantum Zeno effect [141]. Comparing the different phonon excitation probabilities in Fig. 8 then suggests that for dissipation-generated anharmonicities, there is an increasing number of non-projective measurements corresponding to phonons dissipating to the environment, which strongly suppresses the transport of bipolarons.

4 Conclusion

Incorporating dissipation into the description of strongly-correlated electron systems coupled to phonons paved the way to intriguing phenomena such as light-enhanced or cavity-induced phonon-mediated superconductivity [142–144]. Furthermore, in the prototypical Hubbard-Holstein model, recent (semi-) analytical investigations suggested the enhancement of the metallic regime in the presence of anharmonic phonons, posing the question of enhanced superconducting correlations [16, 138, 139]. In this study, we therefore investigated the effect of a realistic source of phonon anharmonicities generated by a dissipative coupling of the phonons to an environment.

In order to be able to perform the required, numerically very challenging, dissipative quantum many-body simulations for large systems we combined both HOPS and QJ, two established out-of equilibrium methods to describe OQS, with the recently introduced PP-DMRG. We tested and benchmarked the obtained numerical tools, demonstrating their feasibility in capturing the complex, dissipative out-of equilibrium dynamics after global quenches.

Interestingly, we found that both methods, being comparably computationally efficient, exhibit complementary regimes of the physical model parameter in which they yield precise and numerically well-controlled time-evolution schemes. In particular, HOPS proved to be the method of choice for the case of intermediate and strong dissipation and large electron-phonon couplings, whereas QJ yielded excellent performance for weak dissipation and weak to intermediate electron-phonon couplings. As a consequence, using the PP-mapping, we elevated OQS methods to be applicable in an efficient and unbiased way to a broad class of dissipative quantum many-body systems, using tensor network algorithms. We believe that the discussed, tensor network-based Markovian (QJ) and non-Markovian (HOPS) methods will be very fruitful tools for addressing relevant problems such as thermalization of quantum systems [145–147], cooling of quantum many-body systems [148, 149], exciton dynamics in light-harvesting complexes [150, 151], and quantum transport in two-terminal dissipative setups [152–157]. Moreover, as mentioned in App. B, the methods developed here for systems described by Eqs. (1) and (2), can be generalized to multiple phonon modes per site, to phonon modes coupled to baths with arbitrary spectral structures, or to non-local phonons coupled to several sites [158]. This latter generalization could, for instance, make it possible to study dissipative versions of the Hubbard-Fröhlich model [159, 160].

Having established the PP-enhanced HOPS and QJ methods, we turned to the question of whether dissipation enhances metallicity in the Hubbard-Holstein model. For that purpose, we performed a series of quenches, investigating the formation of bipolarons, i.e., phonon-mediated bound two-electron quasi-particles and their metallicity. Here, we defined metallicity as the ratio between the bipolaronic binding energy and its effective mass. In the metallic regime of the Hubbard-Holstein ground-state phase diagram, we found that the time dependence of the bipolaronic binding energy remains mainly unchanged, i.e., the phonons that contribute to bound electron pairs do not tend to escape the system. Studying the bipolaronic kinetic energy dynamics, we observed melting of the bipolaronic single-particle gap upon increasing dissipation, indicating an increased scattering rate. Consequently, the effect of dissipation is to enhance the bipolaronic effective mass, yielding an overall reduction of the bipolaronic metallicity. Since our results contrast previous findings when considering gaussian anharmonicities, we calculated the phononic excitation probabilities for the different sources of anharmonic phonons. We show that the effect of a gaussian anharmonicity is to reduce the decay of the excitation probabilities compared to the harmonic situation. In contrast, dissipation has the opposite effect, generating a quick decay of the phonon excitation probabilities. Here, the picture of a quantum jump description of the dissipative dynamics creates an interesting connection to the quantum Zeno effect [141, 161]. The rapid decay of phononic excitation probabilities suggests a significant rate of jump events of phonons from the system into the environment, even at moderate dissipation strengths. These jump events can be interpreted as local measurements, which suppress the delocalization of the bipolaronic quasi-particles.

Nevertheless, we also find that the bipolaronic binding energy is very robust against dissipation in the metallic regime. This is a remarkable observation, in particular, since the calculated binding energies are of the order of $0.15\,J$ and thereby much smaller than the studied dissipation strengths $\kappa = 1J$, $4J$. Understanding the origin of this unexpected robustness of formed bipolarons in the metallic regime would be an interesting theoretical question, particularly concerning phonon-mediated superconductivity. Furthermore, our results imply that the various sources of phonon-anharmonicities need to be considered very thoroughly when deriving effective, microscopic models for real materials. In particular, the question arises

of what happens if competing effects such as gaussian anharmonicities and dissipation exist. Here, further investigations are indispensable and may especially address the question of whether the robustness of the bipolarons can carry over to the case of intrinsic material sources of anharmonicities.

References

[1] J. G. Bednorz and K. A. Müller, Possible high tc superconductivity in the ba-la-cu-o system, Zeitschrift für Physik B Condensed Matter **64**(2), 189 (1986), doi:10.1007/BF01303701.

[2] M. K. Wu, J. R. Ashburn, C. J. Torng, P. H. Hor, R. L. Meng, L. Gao, Z. J. Huang, Y. Q. Wang and C. W. Chu, Superconductivity at 93 k in a new mixed-phase y-ba-cu-o compound system at ambient pressure, Phys. Rev. Lett. **58**, 908 (1987), doi:10.1103/PhysRevLett.58.908.

[3] E. Dagotto, Correlated electrons in high-temperature superconductors, Rev. Mod. Phys. **66**, 763 (1994), doi:10.1103/RevModPhys.66.763.

[4] P. A. Lee, N. Nagaosa and X.-G. Wen, Doping a mott insulator: Physics of high-temperature superconductivity, Rev. Mod. Phys. **78**, 17 (2006), doi:10.1103/RevModPhys.78.17.

[5] K. Miyake, S. Schmitt-Rink and C. M. Varma, Spin-fluctuation-mediated even-parity pairing in heavy-fermion superconductors, Phys. Rev. B **34**, 6554 (1986), doi:10.1103/PhysRevB.34.6554.

[6] F. C. Zhang and T. M. Rice, Effective hamiltonian for the superconducting cu oxides, Phys. Rev. B **37**, 3759 (1988), doi:10.1103/PhysRevB.37.3759.

[7] M. Tsuchiizu and A. Furusaki, Phase diagram of the one-dimensional extended hubbard model at half filling, Physical Review Letters **88**(5) (2002), doi:10.1103/physrevlett.88.056402.

[8] R. M. Lutchyn, J. D. Sau and S. D. Sarma, Majorana fermions and a topological phase transition in semiconductor-superconductor heterostructures, Physical Review Letters **105**(7) (2010), doi:10.1103/physrevlett.105.077001.

[9] M. H. Fischer, T. Neupert, C. Platt, A. P. Schnyder, W. Hanke, J. Goryo, R. Thomale and M. Sigrist, Chiral d-wave superconductivity in srptas, Phys. Rev. B **89**, 020509 (2014), doi:10.1103/PhysRevB.89.020509.

[10] M. Jourdan, M. Huth and H. Adrian, Superconductivity mediated by spin fluctuations in the heavy-fermion compound upd2 al3, Nature **398**(6722), 47 (1999), doi:10.1038/17977.

[11] M. Tezuka, R. Arita and H. Aoki, Phase diagram for the one-dimensional hubbard-holstein model: A density-matrix renormalization group study, Phys. Rev. B **76**, 155114 (2007), doi:10.1103/PhysRevB.76.155114.

[12] A. Macridin and M. Jarrell, Isotope effect in the hubbard model with local phonons, Phys. Rev. B **79**, 104517 (2009), doi:10.1103/PhysRevB.79.104517.

[13] F. Marsiglio, Impact of retardation in the holstein-hubbard model: a two-site calculation, doi:10.48550/ARXIV.2205.10352 (2022).

[14] O. S. Barišić and S. Barišić, Bipolarons and polarons in the holstein-hubbard model: analogies and differences, The European Physical Journal B **85**(3) (2012), doi:10.1140/epjb/e2012-21079-2.

[15] J. Sous, M. Chakraborty, R. V. Krems and M. Berciu, Light bipolarons stabilized by peierls electron-phonon coupling, Phys. Rev. Lett. **121**, 247001 (2018), doi:10.1103/PhysRevLett.121.247001.

[16] C. U. Lavanya, I. V. Sankar and A. Chatterjee, Metallicity in a holstein-hubbard chain at half filling with gaussian anharmonicity, Scientific Reports **7**(1), 3774 (2017), doi:10.1038/s41598-017-03985-2.

[17] D. Debnath, M. Z. Malik and A. Chatterjee, A semi exact solution for a metallic phase in a holstein-hubbard chain at half filling with gaussian anharmonic phonons, Scientific Reports **11**(1), 12305 (2021), doi:10.1038/s41598-021-91604-6.

[18] N. C. Costa, T. Blommel, W.-T. Chiu, G. Batrouni and R. T. Scalettar, Phonon dispersion and the competition between pairing and charge order, Phys. Rev. Lett. **120**, 187003 (2018), doi:10.1103/PhysRevLett.120.187003.

[19] D. Jansen, J. Bonča and F. Heidrich-Meisner, Finite-temperature optical conductivity with density-matrix renormalization group methods for the holstein polaron and bipolaron with dispersive phonons, doi:10.48550/ARXIV.2206.00985 (2022).

[20] S. R. White, Density matrix formulation for quantum renormalization groups, Phys. Rev. Lett. **69**(19), 2863 (1992), doi:10.1103/PhysRevLett.69.2863.

[21] S. R. White, Density-matrix algorithms for quantum renormalization groups, Phys. Rev. B **48**(14), 10345 (1993), doi:10.1103/PhysRevB.48.10345.

[22] U. Schollwöck, The density-matrix renormalization group, Reviews of Modern Physics **77**(1), 259–315 (2005), doi:10.1103/revmodphys.77.259.

[23] U. Schollwöck, The density-matrix renormalization group in the age of matrix product states, Annals of Physics **326**(1), 96–192 (2011), doi:10.1016/j.aop.2010.09.012.

[24] E. Jeckelmann and S. R. White, Density-matrix renormalization-group study of the polaron problem in the holstein model, Phys. Rev. B **57**, 6376 (1998), doi:10.1103/PhysRevB.57.6376.

[25] H. Benthien, F. Gebhard and E. Jeckelmann, Spectral function of the one-dimensional hubbard model away from half filling, Phys. Rev. Lett. **92**, 256401 (2004), doi:10.1103/PhysRevLett.92.256401.

[26] F. Heidrich-Meisner, A. Honecker and T. Vekua, Frustrated ferromagnetic spin-$\frac{1}{2}$ chain in a magnetic field: The phase diagram and thermodynamic properties, Phys. Rev. B **74**, 020403 (2006), doi:10.1103/PhysRevB.74.020403.

[27] S. Yan, D. A. Huse and S. R. White, Spin-liquid ground state of the ¡i¿s¡/i¿ = 1/2 kagome heisenberg antiferromagnet, Science **332**(6034), 1173 (2011), doi:10.1126/science.1201080, https://www.science.org/doi/pdf/10.1126/science.1201080.

[28] A. Holzner, A. Weichselbaum, I. P. McCulloch, U. Schollwöck and J. von Delft, Chebyshev matrix product state approach for spectral functions, Phys. Rev. B **83**, 195115 (2011), doi:10.1103/PhysRevB.83.195115.

[29] S. Depenbrock, I. P. McCulloch and U. Schollwöck, Nature of the spin-liquid ground state of the $s = 1/2$ heisenberg model on the kagome lattice, Phys. Rev. Lett. **109**, 067201 (2012), doi:10.1103/PhysRevLett.109.067201.

[30] T. Shirakawa, T. Tohyama, J. Kokalj, S. Sota and S. Yunoki, Ground-state phase diagram of the triangular lattice hubbard model by the density-matrix renormalization group method, Phys. Rev. B **96**, 205130 (2017), doi:10.1103/PhysRevB.96.205130.

[31] B.-X. Zheng, C.-M. Chung, P. Corboz, G. Ehlers, M.-P. Qin, R. M. Noack, H. Shi, S. R. White, S. Zhang and G. K.-L. Chan, Stripe order in the underdoped region of the two-dimensional hubbard model, Science **358**(6367), 1155 (2017), doi:10.1126/science.aam7127, https://www.science.org/doi/pdf/10.1126/science.aam7127.

[32] E. Jeckelmann, Dynamical density-matrix renormalization-group method, Phys. Rev. B **66**, 045114 (2002), doi:10.1103/PhysRevB.66.045114.

[33] A. M. Läuchli and C. Kollath, Spreading of correlations and entanglement after a quench in the one-dimensional bose–hubbard model, Journal of Statistical Mechanics: Theory and Experiment **2008**(05), P05018 (2008), doi:10.1088/1742-5468/2008/05/p05018.

[34] S. Langer, F. Heidrich-Meisner, J. Gemmer, I. P. McCulloch and U. Schollwöck, Real-time study of diffusive and ballistic transport in spin-$\frac{1}{2}$ chains using the adaptive time-dependent density matrix renormalization group method, Phys. Rev. B **79**, 214409 (2009), doi:10.1103/PhysRevB.79.214409.

[35] S. R. Manmana, S. Wessel, R. M. Noack and A. Muramatsu, Time evolution of correlations in strongly interacting fermions after a quantum quench, Phys. Rev. B **79**, 155104 (2009), doi:10.1103/PhysRevB.79.155104.

[36] C. Karrasch and D. Schuricht, Dynamical phase transitions after quenches in nonintegrable models, Phys. Rev. B **87**, 195104 (2013), doi:10.1103/PhysRevB.87.195104.

[37] F. H. L. Essler, S. Kehrein, S. R. Manmana and N. J. Robinson, Quench dynamics in a model with tuneable integrability breaking, Phys. Rev. B **89**, 165104 (2014), doi:10.1103/PhysRevB.89.165104.

[38] S. Sorg, L. Vidmar, L. Pollet and F. Heidrich-Meisner, Relaxation and thermalization in the one-dimensional bose-hubbard model: A case study for the interaction quantum quench from the atomic limit, Phys. Rev. A **90**, 033606 (2014), doi:10.1103/PhysRevA.90.033606.

[39] F. Schwarz, I. Weymann, J. von Delft and A. Weichselbaum, Nonequilibrium steady-state transport in quantum impurity models: A thermofield and quantum quench approach using matrix product states, Phys. Rev. Lett. **121**, 137702 (2018), doi:10.1103/PhysRevLett.121.137702.

[40] S. Paeckel, T. Köhler, A. Swoboda, S. R. Manmana, U. Schollwöck and C. Hubig, Time-evolution methods for matrix-product states, Annals of Physics **411**, 167998 (2019), doi:10.1016/j.aop.2019.167998.

[41] S. Paeckel, B. Fauseweh, A. Osterkorn, T. Köhler, D. Manske and S. R. Manmana, Detecting superconductivity out of equilibrium, Phys. Rev. B **101**, 180507 (2020), doi:10.1103/PhysRevB.101.180507.

[42] Q. Tang and W. Zhu, Measurement-induced phase transition: A case study in the nonintegrable model by density-matrix renormalization group calculations, Phys. Rev. Research **2**, 013022 (2020), doi:10.1103/PhysRevResearch.2.013022.

[43] D. J. García, K. Hallberg and M. J. Rozenberg, Dynamical mean field theory with the density matrix renormalization group, Phys. Rev. Lett. **93**, 246403 (2004), doi:10.1103/PhysRevLett.93.246403.

[44] F. Güttge, F. B. Anders, U. Schollwöck, E. Eidelstein and A. Schiller, Hybrid nrg-dmrg approach to real-time dynamics of quantum impurity systems, Phys. Rev. B **87**, 115115 (2013), doi:10.1103/PhysRevB.87.115115.

[45] H. Aoki, N. Tsuji, M. Eckstein, M. Kollar, T. Oka and P. Werner, Nonequilibrium dynamical mean-field theory and its applications, Rev. Mod. Phys. **86**, 779 (2014), doi:10.1103/RevModPhys.86.779.

[46] F. A. Wolf, I. P. McCulloch, O. Parcollet and U. Schollwöck, Chebyshev matrix product state impurity solver for dynamical mean-field theory, Phys. Rev. B **90**, 115124 (2014), doi:10.1103/PhysRevB.90.115124.

[47] F. A. Wolf, A. Go, I. P. McCulloch, A. J. Millis and U. Schollwöck, Imaginary-time matrix product state impurity solver for dynamical mean-field theory, Phys. Rev. X **5**, 041032 (2015), doi:10.1103/PhysRevX.5.041032.

[48] M. Bramberger, J. Mravlje, M. Grundner, U. Schollwöck and M. Zingl, baoso$_3$: A hund's metal in the presence of strong spin-orbit coupling, Phys. Rev. B **103**, 165133 (2021), doi:10.1103/PhysRevB.103.165133.

[49] S. R. White and R. L. Martin, Ab initio quantum chemistry using the density matrix renormalization group, The Journal of Chemical Physics **110**(9), 4127 (1999), doi:10.1063/1.478295, https://doi.org/10.1063/1.478295.

[50] K. H. Marti and M. Reiher, The density matrix renormalization group algorithm in quantum chemistry, Zeitschrift für Physikalische Chemie **224**(3-4), 583 (2010), doi:doi:10.1524/zpch.2010.6125.

[51] N. Lin, C. A. Marianetti, A. J. Millis and D. R. Reichman, Dynamical mean-field theory for quantum chemistry, Phys. Rev. Lett. **106**, 096402 (2011), doi:10.1103/PhysRevLett.106.096402.

[52] S. Wouters and D. Van Neck, The density matrix renormalization group for ab initio quantum chemistry, The European Physical Journal D **68**(9), 272 (2014), doi:10.1140/epjd/e2014-50500-1.

[53] X. Xie, Y. Liu, Y. Yao, U. Schollwöck, C. Liu and H. Ma, Time-dependent density matrix renormalization group quantum dynamics for realistic chemical systems, The Journal of Chemical Physics **151**(22), 224101 (2019), doi:10.1063/1.5125945, https://doi.org/10.1063/1.5125945.

[54] S. Mardazad, Y. Xu, X. Yang, M. Grundner, U. Schollwöck, H. Ma and S. Paeckel, Quantum dynamics simulation of intramolecular singlet fission in covalently linked tetracene dimer, The Journal of Chemical Physics **155**(19), 194101 (2021), doi:10.1063/5.0068292.

[55] I. Lesanovsky, M. van Horssen, M. u. u. u. u. Guţă and J. P. Garrahan, Characterization of dynamical phase transitions in quantum jump trajectories beyond the properties of the stationary state, Phys. Rev. Lett. **110**, 150401 (2013), doi:10.1103/PhysRevLett.110.150401.

[56] I. de Vega and M.-C. Bañuls, Thermofield-based chain-mapping approach for open quantum systems, Phys. Rev. A **92**, 052116 (2015), doi:10.1103/PhysRevA.92.052116.

[57] F. A. Y. N. Schröder and A. W. Chin, Simulating open quantum dynamics with time-dependent variational matrix product states: Towards microscopic correlation of environment dynamics and reduced system evolution, Phys. Rev. B **93**, 075105 (2016), doi:10.1103/PhysRevB.93.075105.

[58] S. Wolff, A. Sheikhan and C. Kollath, Numerical evaluation of two-time correlation functions in open quar SciPost Phys. Core **3**, 10 (2020), doi:10.21468/SciPostPhysCore.3.2.010.

[59] A. Nüßeler, I. Dhand, S. F. Huelga and M. B. Plenio, Efficient simulation of open quantum systems coupled to a fermionic bath, Phys. Rev. B **101**, 155134 (2020), doi:10.1103/PhysRevB.101.155134.

[60] M. Reh, M. Schmitt and M. Gärttner, Time-dependent variational principle for open quantum systems with artificial neural networks, Phys. Rev. Lett. **127**, 230501 (2021), doi:10.1103/PhysRevLett.127.230501.

[61] G. Kordas, D. Witthaut, P. Buonsante, A. Vezzani, R. Burioni, A. I. Karanikas and S. Wimberger, The dissipative bose-hubbard model, The European Physical Journal Special Topics **224**(11), 2127 (2015), doi:10.1140/epjst/e2015-02528-2.

[62] A. J. Daley, J. M. Taylor, S. Diehl, M. Baranov and P. Zoller, Atomic three-body loss as a dynamical three-body interaction, Phys. Rev. Lett. **102**, 040402 (2009), doi:10.1103/PhysRevLett.102.040402.

[63] A. Kantian, M. Dalmonte, S. Diehl, W. Hofstetter, P. Zoller and A. J. Daley, Atomic color superfluid via three-body loss, Physical Review Letters **103**(24) (2009), doi:10.1103/physrevlett.103.240401.

[64] P. Barmettler and C. Kollath, Controllable manipulation and detection of local densities and bipartite entanglement in a quantum gas by a dissipative defect, Phys. Rev. A **84**, 041606 (2011), doi:10.1103/PhysRevA.84.041606.

[65] L. Bonnes and A. M. Lauchli, Superoperators vs. trajectories for matrix product state simulations of open quantum system: A case study, arXiv: Quantum Gases (2014).

[66] J. Cui, J. I. Cirac and M. C. Bañuls, Variational matrix product operators for the steady state of dissipative quantum systems, Physical Review Letters **114**(22) (2015), doi:10.1103/physrevlett.114.220601.

[67] H. Pichler, A. J. Daley and P. Zoller, Nonequilibrium dynamics of bosonic atoms in optical lattices: Decoherence of many-body states due to spontaneous emission, Physical Review A **82**(6) (2010), doi:10.1103/physreva.82.063605.

[68] J. Schachenmayer, L. Pollet, M. Troyer and A. J. Daley, Spontaneous emission and thermalization of cold bosons in optical lattices, Phys. Rev. A **89**, 011601 (2014), doi:10.1103/PhysRevA.89.011601.

[69] I. de Vega and D. Alonso, Dynamics of non-markovian open quantum systems, Rev. Mod. Phys. **89**, 015001 (2017), doi:10.1103/RevModPhys.89.015001.

[70] U. Weiss, Quantum Dissipative Systems, World Scientific (2012).

[71] M. H. Anderson, J. R. Ensher, M. R. Matthews, C. E. Wieman and E. A. Cornell, Observation of bose-einstein condensation in a dilute atomic vapor, Science **269**(5221), 198 (1995), doi:10.1126/science.269.5221.198.

[72] D. Jaksch, C. Bruder, J. I. Cirac, C. W. Gardiner and P. Zoller, Cold bosonic atoms in optical lattices, Phys. Rev. Lett. **81**(15), 3108–3111 (1998), doi:10.1103/physrevlett.81.3108.

[73] I. Bloch, J. Dalibard and W. Zwerger, Many-body physics with ultracold gases, Rev. Mod. Phys. **80**, 885 (2008), doi:10.1103/RevModPhys.80.885.

[74] L.-K. Lim, C. M. Smith and A. Hemmerich, Staggered-vortex superfluid of ultracold bosons in an optical lattice, Phys. Rev. Lett. **100**, 130402 (2008), doi:10.1103/PhysRevLett.100.130402.

[75] Y. N. M. de Escobar, P. G. Mickelson, M. Yan, B. J. Desalvo, S. B. Nagel and T. C. Killian, Bose-einstein condensation of sr84, Phys. Rev. Lett. **103**, 200402 (2009), doi:10.1103/PhysRevLett.103.200402.

[76] I. B. Mekhov, C. Maschler and H. Ritsch, Probing quantum phases of ultracold atoms in optical lattices by transmission spectra in cavity quantum electrodynamics, Nature Physics **3**(5), 319 (2007), doi:10.1038/nphys571.

[77] K. W. Murch, K. L. Moore, S. Gupta and D. M. Stamper-Kurn, Observation of quantum-measurement backaction with an ultracold atomic gas, Nature Physics **4**(7), 561 (2008), doi:10.1038/nphys965.

[78] S. Gröblacher, J. B. Hertzberg, M. R. Vanner, G. D. Cole, S. Gigan, K. C. Schwab and M. Aspelmeyer, Demonstration of an ultracold micro-optomechanical oscillator in a cryogenic cavity, Nature Physics **5**(7), 485 (2009), doi:10.1038/nphys1301.

[79] J. Verdú, H. Zoubi, C. Koller, J. Majer, H. Ritsch and J. Schmiedmayer, Strong magnetic coupling of an ultracold gas to a superconducting waveguide cavity, Phys. Rev. Lett. **103**, 043603 (2009), doi:10.1103/PhysRevLett.103.043603.

[80] T. P. Purdy, D. W. C. Brooks, T. Botter, N. Brahms, Z.-Y. Ma and D. M. Stamper-Kurn, Tunable cavity optomechanics with ultracold atoms, Phys. Rev. Lett. **105**, 133602 (2010), doi:10.1103/PhysRevLett.105.133602.

[81] C. Kollath, A. Sheikhan, S. Wolff and F. Brennecke, Ultracold fermions in a cavity-induced artificial magnetic field, Phys. Rev. Lett. **116**, 060401 (2016), doi:10.1103/PhysRevLett.116.060401.

[82] E. Thyrhaug, K. Žídek, J. Dostál, D. Bína and D. Zigmantas, Exciton structure and energy transfer in the fenna–matthews–olson complex, The Journal of Physical Chemistry Letters **7**(9), 1653 (2016), doi:10.1021/acs.jpclett.6b00534, PMID: 27082631, https://doi.org/10.1021/acs.jpclett.6b00534.

[83] Y. Zhang, L. Yu, J.-Q. Liang, G. Chen, S. Jia and F. Nori, Quantum phases in circuit qed with a superconducting qubit array, Scientific Reports **4**(1), 4083 (2014), doi:10.1038/srep04083.

[84] P. Krantz, M. Kjaergaard, F. Yan, T. P. Orlando, S. Gustavsson and W. D. Oliver, A quantum engineer's guide to superconducting qubits, Applied Physics Reviews **6**(2), 021318 (2019), doi:10.1063/1.5089550.

[85] F. Arute, K. Arya, R. Babbush, D. Bacon, J. C. Bardin, R. Barends, R. Biswas, S. Boixo, F. G. S. L. Brandao, D. A. Buell, B. Burkett, Y. Chen et al., Quantum supremacy using a programmable superconducting processor, Nature **574**(7779), 505 (2019), doi:10.1038/s41586-019-1666-5.

[86] D. R. W. Yost, M. E. Schwartz, J. Mallek, D. Rosenberg, C. Stull, J. L. Yoder, G. Calusine, M. Cook, R. Das, A. L. Day, E. B. Golden, D. K. Kim et al., Solid-state qubits integrated with superconducting through-silicon vias, npj Quantum Information **6**(1), 59 (2020), doi:10.1038/s41534-020-00289-8.

[87] Y. Zhou, E. M. Stoudenmire and X. Waintal, What limits the simulation of quantum computers?, Phys. Rev. X **10**, 041038 (2020), doi:10.1103/PhysRevX.10.041038.

[88] F. Fedele, A. Chatterjee, S. Fallahi, G. C. Gardner, M. J. Manfra and F. Kuemmeth, Simultaneous operations in a two-dimensional array of singlet-triplet qubits, PRX Quantum **2**, 040306 (2021), doi:10.1103/PRXQuantum.2.040306.

[89] M. McEwen, L. Faoro, K. Arya, A. Dunsworth, T. Huang, S. Kim, B. Burkett, A. Fowler, F. Arute, J. C. Bardin, A. Bengtsson, A. Bilmes et al., Resolving catastrophic error bursts from cosmic rays in large arrays of superconducting qubits, Nature Physics **18**(1), 107 (2022), doi:10.1038/s41567-021-01432-8.

[90] A. Strathearn, P. Kirton, D. Kilda, J. Keeling and B. W. Lovett, Efficient non-markovian quantum dynamics using time-evolving matrix product operators, Nature Communications **9**(1) (2018), doi:10.1038/s41467-018-05617-3.

[91] R. Finsterhölzl, M. Katzer, A. Knorr and A. Carmele, Using matrix-product states for open quantum many-body systems: Efficient algorithms for markovian and non-markovian time-evolution, Entropy **22**(9) (2020), doi:10.3390/e22090984.

[92] N. Lambert, T. Raheja, S. Ahmed, A. Pitchford and F. Nori, Bofin-heom: A bosonic and fermionic numerical hierarchical-equations-of-motion library with applications in light-harvesting, quantum control, and single-molecule electronics, doi:10.48550/ARXIV.2010.10806 (2020).

[93] S. Flannigan, F. Damanet and A. J. Daley, Many-body quantum state diffusion for non-markovian dynamics in strongly interacting systems, Phys. Rev. Lett. **128**, 063601 (2022), doi:10.1103/PhysRevLett.128.063601.

[94] X. Gao, J. Ren, A. Eisfeld and Z. Shuai, Non-markovian stochastic schrödinger equation: Matrix-product-state approach to the hierarchy of pure states, Physical Review A **105**(3) (2022), doi:10.1103/physreva.105.l030202.

[95] Y. Tanimura and R. Kubo, Time evolution of a quantum system in contact with a nearly gaussian-markoffian noise bath, Journal of the Physical Society of Japan **58**(1), 101 (1989), doi:10.1143/JPSJ.58.101, https://doi.org/10.1143/JPSJ.58.101.

[96] Y. Tanimura, Nonperturbative expansion method for a quantum system coupled to a harmonic-oscillator bath, Phys. Rev. A **41**, 6676 (1990), doi:10.1103/PhysRevA.41.6676.

[97] T. Köhler, J. Stolpp and S. Paeckel, Efficient and flexible approach to simulate low-dimensional quantum lattice models with large local hilbert spaces, SciPost Physics **10**(3) (2021), doi:10.21468/scipostphys.10.3.058.

[98] J. Stolpp, T. Köhler, S. R. Manmana, E. Jeckelmann, F. Heidrich-Meisner and S. Paeckel, Comparative study of state-of-the-art matrix-product-state methods for lattice models with large local hilbert spaces without u(1) symmetry, Computer Physics Communications **269**, 108106 (2021), doi:10.1016/j.cpc.2021.108106.

[99] D. Suess, A. Eisfeld and W. T. Strunz, Hierarchy of stochastic pure states for open quantum system dynamics, Phys. Rev. Lett. **113**, 150403 (2014), doi:10.1103/PhysRevLett.113.150403.

[100] A. J. Daley, Quantum trajectories and open many-body quantum systems, Advances in Physics **63**(2), 77–149 (2014), doi:10.1080/00018732.2014.933502.

[101] P. Pearle, Simple derivation of the lindblad equation, European Journal of Physics **33**(4), 805 (2012), doi:10.1088/0143-0807/33/4/805.

[102] L. Diósi and W. T. Strunz, The non-markovian stochastic schrödinger equation for open systems, Physics Letters A **235**(6), 569 (1997), doi:10.1016/s0375-9601(97)00717-2.

[103] R. Hartmann and W. T. Strunz, Exact open quantum system dynamics using the hierarchy of pure states (hops), Journal of Chemical Theory and Computation **13**(12), 5834–5845 (2017), doi:10.1021/acs.jctc.7b00751.

[104] D. Suess, W. T. Strunz and A. Eisfeld, Hierarchical equations for open system dynamics in fermionic and bosonic environments, Journal of Statistical Physics **159**(6), 1408 (2015), doi:10.1007/s10955-015-1236-7.

[105] F. Verstraete, J. J. García-Ripoll and J. I. Cirac, Matrix product density operators: Simulation of finite-temperature and dissipative systems, Phys. Rev. Lett. **93**, 207204 (2004), doi:10.1103/PhysRevLett.93.207204.

[106] S. Rommer and S. Östlund, Class of ansatz wave functions for one-dimensional spin systems and their relation to the density matrix renormalization group, Phys. Rev. B **55**, 2164 (1997), doi:10.1103/PhysRevB.55.2164.

[107] G. Vidal, Entanglement renormalization, Phys. Rev. Lett. **99**, 220405 (2007), doi:10.1103/PhysRevLett.99.220405.

[108] G. Vidal, Efficient simulation of one-dimensional quantum many-body systems, Phys. Rev. Lett. **93**, 040502 (2004), doi:10.1103/PhysRevLett.93.040502.

[109] R. Orús, A practical introduction to tensor networks: Matrix product states and projected entangled pair states, Annals of Physics **349**, 117–158 (2014), doi:10.1016/j.aop.2014.06.013.

[110] J. Haegeman, J. I. Cirac, T. J. Osborne, I. Pižorn, H. Verschelde and F. Verstraete, Time-dependent variational principle for quantum lattices, Phys. Rev. Lett. **107**, 070601 (2011), doi:10.1103/PhysRevLett.107.070601.

[111] J. Haegeman, C. Lubich, I. Oseledets, B. Vandereycken and F. Verstraete, Unifying time evolution and optimization with matrix product states, Phys. Rev. B **94**, 165116 (2016), doi:10.1103/PhysRevB.94.165116.

[112] M. P. Zaletel, R. S. K. Mong, C. Karrasch, J. E. Moore and F. Pollmann, Time-evolving a matrix product state with long-ranged interactions, Phys. Rev. B **91**, 165112 (2015), doi:10.1103/PhysRevB.91.165112.

[113] M. Suzuki, General decomposition theory of ordered exponentials, Proceedings of the Japan Academy, Series B **69**(7), 161 (1993).

[114] C. Brockt, F. Dorfner, L. Vidmar, F. Heidrich-Meisner and E. Jeckelmann, Matrix-product-state method with a dynamical local basis optimization for bosonic systems out of equilibrium, Phys. Rev. B **92**, 241106 (2015), doi:10.1103/PhysRevB.92.241106.

[115] R. J. Bursill, Density-matrix renormalization-group algorithm for quantum lattice systems with a large number of states per site, Phys. Rev. B **60**, 1643 (1999), doi:10.1103/PhysRevB.60.1643.

[116] B. Friedman, Optimal phonon approach to the spin peierls model with nonadiabatic spin-phonon coupling, Phys. Rev. B **61**, 6701 (2000), doi:10.1103/PhysRevB.61.6701.

[117] H. Wong and Z.-D. Chen, Density matrix renormalization group approach to the spin-boson model, Phys. Rev. B **77**, 174305 (2008), doi:10.1103/PhysRevB.77.174305.

[118] S. Singh, R. N. C. Pfeifer and G. Vidal, Tensor network decompositions in the presence of a global symmetry, Phys. Rev. A **82**, 050301 (2010), doi:10.1103/PhysRevA.82.050301.

[119] T. Holstein, Studies of polaron motion: Part I. The molecular-crystal model, Ann. Phys. **8**(3), 325 (1959), doi:10.1016/0003-4916(59)90002-8.

[120] A. F. Hebard, M. J. Rosseinsky, R. C. Haddon, D. W. Murphy, S. H. Glarum, T. T. M. Palstra, A. P. Ramirez and A. R. Kortan, Superconductivity at 18 k in potassium-doped c60, Nature **350**(6319), 600 (1991), doi:10.1038/350600a0.

[121] K. Tanigaki, T. W. Ebbesen, S. Saito, J. Mizuki, J. S. Tsai, Y. Kubo and S. Kuroshima, Superconductivity at 33 k in csxrbyc60, Nature **352**(6332), 222 (1991), doi:10.1038/352222a0.

[122] M. Mitrano, A. Cantaluppi, D. Nicoletti, S. Kaiser, A. Perucchi, S. Lupi, P. Di Pietro, D. Pontiroli, M. Riccò, S. R. Clark, D. Jaksch and A. Cavalleri, Possible light-induced superconductivity in k3c60 at high temperature, Nature **530**(7591), 461 (2016), doi:10.1038/nature16522.

[123] A. Nava, C. Giannetti, A. Georges, E. Tosatti and M. Fabrizio, Cooling quasiparticles in a3c60 fullerides by excitonic mid-infrared absorption, Nature Physics **14**(2), 154 (2018), doi:10.1038/nphys4288.

[124] M. Budden, T. Gebert, M. Buzzi, G. Jotzu, E. Wang, T. Matsuyama, G. Meier, Y. Laplace, D. Pontiroli, M. Riccò, F. Schlawin, D. Jaksch et al., Evidence for metastable photo-induced superconductivity in k3c60, Nature Physics **17**(5), 611 (2021), doi:10.1038/s41567-020-01148-1.

[125] R. T. Clay and R. P. Hardikar, Intermediate phase of the one dimensional half-filled hubbard-holstein model, Phys. Rev. Lett. **95**, 096401 (2005), doi:10.1103/PhysRevLett.95.096401.

[126] W.-Q. Ning, H. Zhao, C.-Q. Wu and H.-Q. Lin, *Phonon effects on spin-charge separation in one dimension*, Phys. Rev. Lett. **96**, 156402 (2006), doi:10.1103/PhysRevLett.96.156402.

[127] M. Weber, F. F. Assaad and M. Hohenadler, *Phonon spectral function of the one-dimensional holstein-hubbard model*, Phys. Rev. B **91**, 235150 (2015), doi:10.1103/PhysRevB.91.235150.

[128] T. E. Reinhard, U. Mordovina, C. Hubig, J. S. Kretchmer, U. Schollwöck, H. Appel, M. A. Sentef and A. Rubio, *Density-matrix embedding theory study of the one-dimensional hubbard–holstein model*, Journal of Chemical Theory and Computation **15**(4), 2221 (2019), doi:10.1021/acs.jctc.8b01116.

[129] J. Stolpp, J. Herbrych, F. Dorfner, E. Dagotto and F. Heidrich-Meisner, *Charge-density-wave melting in the one-dimensional holstein model*, Phys. Rev. B **101**, 035134 (2020), doi:10.1103/PhysRevB.101.035134.

[130] D. Jansen, C. Jooss and F. Heidrich-Meisner, *Charge density wave breakdown in a heterostructure with electron-phonon coupling*, Physical Review B **104**(19) (2021), doi:10.1103/physrevb.104.195116.

[131] M. t. Brink, S. Gräber, M. Hopjan, D. Jansen, J. Stolpp, F. Heidrich-Meisner and P. E. Blöchl, *Real-time non-adiabatic dynamics in the one-dimensional holstein model: trajectory-based versus exact methods*, doi:10.48550/ARXIV.2203.07245 (2022).

[132] Y. Takada and A. Chatterjee, *Possibility of a metallic phase in the charge-density-wave–spin-density-wave crossover region in the one-dimensional hubbard-holstein model at half filling*, Phys. Rev. B **67**, 081102 (2003), doi:10.1103/PhysRevB.67.081102.

[133] W. Koller, D. Meyer, A. Hewson and Y. Ōno, *Phase diagram and dynamic response functions of the holstein–hubbard model*, Physica B: Condensed Matter **359-361**, 795 (2005), doi:10.1016/j.physb.2005.01.230.

[134] R. P. Hardikar and R. T. Clay, *Phase diagram of the one-dimensional hubbard-holstein model at half and quarter filling*, Phys. Rev. B **75**, 245103 (2007), doi:10.1103/PhysRevB.75.245103.

[135] J. Greitemann, S. Hesselmann, S. Wessel, F. F. Assaad and M. Hohenadler, *Finite-size effects in luther-emery phases of holstein and hubbard models*, Phys. Rev. B **92**, 245132 (2015), doi:10.1103/PhysRevB.92.245132.

[136] S. Mardazad, *Simulating real molecules with tensor network techniques* (2022).

[137] I. Lang and Y. A. Firsov, *Kinetic theory of semiconductors with low mobility*, Sov. Phys. JETP **16**(5), 1301 (1963).

[138] A. Chatterjee and Y. Takada, *The hubbard–holstein model with anharmonic phonons in one dimension*, Journal of the Physical Society of Japan **73**(4), 964 (2004), doi:10.1143/JPSJ.73.964, https://doi.org/10.1143/JPSJ.73.964.

[139] M. Frick, I. Morgenstern and W. von der Linden, <u>High-temperature superconductivity</u> <u>in the apex-oxygen model: a quantum monte carlo study</u>, Zeitschrift für Physik B Condensed Matter **82**, 339 (1991).

[140] E. V. H. Doggen, Y. Gefen, I. V. Gornyi, A. D. Mirlin and D. G. Polyakov, <u>Generalized quantum measurements with matrix product states: Entanglement</u> <u>phase transition and clusterization</u>, Phys. Rev. Research **4**, 023146 (2022), doi:10.1103/PhysRevResearch.4.023146.

[141] B. Yan, S. A. Moses, B. Gadway, J. P. Covey, K. R. A. Hazzard, A. M. Rey, D. S. Jin and J. Ye, <u>Observation of dipolar spin-exchange interactions with lattice-confined polar</u> <u>molecules</u>, Nature **501**(7468), 521 (2013), doi:10.1038/nature12483.

[142] M. A. Sentef, A. F. Kemper, A. Georges and C. Kollath, <u>Theory of</u> <u>light-enhanced phonon-mediated superconductivity</u>, Phys. Rev. B **93**, 144506 (2016), doi:10.1103/PhysRevB.93.144506.

[143] J. B. Curtis, Z. M. Raines, A. A. Allocca, M. Hafezi and V. M. Galitski, <u>Cavity</u> <u>quantum eliashberg enhancement of superconductivity</u>, Phys. Rev. Lett. **122**, 167002 (2019), doi:10.1103/PhysRevLett.122.167002.

[144] F. Schlawin, A. Cavalleri and D. Jaksch, <u>Cavity-mediated</u> <u>electron-photon superconductivity</u>, Phys. Rev. Lett. **122**, 133602 (2019), doi:10.1103/PhysRevLett.122.133602.

[145] L. D'Alessio, Y. Kafri, A. Polkovnikov and M. Rigol, <u>From quantum chaos and</u> <u>eigenstate thermalization to statistical mechanics and thermodynamics</u>, Advances in Physics **65**(3), 239 (2016), doi:10.1080/00018732.2016.1198134.

[146] J. Lebreuilly, A. Chiocchetta and I. Carusotto, <u>Pseudothermalization in</u> <u>driven-dissipative non-markovian open quantum systems</u>, Physical Review A **97**(3) (2018), doi:10.1103/physreva.97.033603.

[147] I. Reichental, A. Klempner, Y. Kafri and D. Podolsky, <u>Thermalization in open quantum</u> <u>systems</u>, Physical Review B **97**(13) (2018), doi:10.1103/physrevb.97.134301.

[148] M. Metcalf, J. E. Moussa, W. A. de Jong and M. Sarovar, <u>Engineered thermalization</u> <u>and cooling of quantum many-body systems</u>, Phys. Rev. Research **2**, 023214 (2020), doi:10.1103/PhysRevResearch.2.023214.

[149] S. Diehl, A. Micheli, A. Kantian, B. Kraus, H. P. Büchler and P. Zoller, <u>Quantum states</u> <u>and phases in driven open quantum systems with cold atoms</u>, Nature Physics **4**(11), 878 (2008), doi:10.1038/nphys1073.

[150] P. Nalbach, D. Braun and M. Thorwart, <u>Exciton transfer dynamics and quantumness of</u> <u>energy transfer in the fenna-matthews-olson complex</u>, Phys. Rev. E **84**, 041926 (2011), doi:10.1103/PhysRevE.84.041926.

[151] E. Thyrhaug, M. Schröter, E. Bukartė, O. Kühn, R. Cogdell, J. Hauer and D. Zigmantas, <u>Intraband dynamics and exciton trapping in the lh2 complex of</u> <u>rhodopseudomonas acidophila</u>, The Journal of Chemical Physics **154**(4), 045102 (2021), doi:10.1063/5.0033802, https://doi.org/10.1063/5.0033802.

[152] F. Damanet, E. Mascarenhas, D. Pekker and A. J. Daley, Reservoir engineering of cooper-pair-assisted transport with cold atoms, New Journal of Physics **21**(11), 115001 (2019), doi:10.1088/1367-2630/ab4f5d.

[153] E. Mascarenhas, F. Damanet, S. Flannigan, L. Tagliacozzo, A. J. Daley, J. Goold and I. de Vega, Nonreciprocal quantum transport at junctions of structured leads, Physical Review B **99**(24) (2019), doi:10.1103/physrevb.99.245134.

[154] F. m. c. Damanet, E. Mascarenhas, D. Pekker and A. J. Daley, Controlling quantum transport via dissipation engineering, Phys. Rev. Lett. **123**, 180402 (2019), doi:10.1103/PhysRevLett.123.180402.

[155] T. Jin, M. Filippone and T. Giamarchi, Generic transport formula for a system driven by markovian reservoirs, Phys. Rev. B **102**, 205131 (2020), doi:10.1103/PhysRevB.102.205131.

[156] A. M. Visuri, T. Giamarchi and C. Kollath, Symmetry-protected transport through a lattice with a local particle loss, doi:10.48550/ARXIV.2201.10286 (2022).

[157] L. Corman, P. Fabritius, S. Häusler, J. Mohan, L. H. Dogra, D. Husmann, M. Lebrat and T. Esslinger, Quantized conductance through a dissipative atomic point contact, Phys. Rev. A **100**, 053605 (2019), doi:10.1103/PhysRevA.100.053605.

[158] Y. Wang, Z. Chen, T. Shi, B. Moritz, Z.-X. Shen and T. P. Devereaux, Phonon-mediated long-range attractive interaction in one-dimensional cuprates, Physical Review Letters **127**(19) (2021), doi:10.1103/physrevlett.127.197003.

[159] A. S. Alexandrov and P. E. Kornilovitch, The fröhlich-coulomb model of high-temperature superconductivity and charge segregation in the cuprates, Journal of Physics: Condensed Matter **14**(21), 5337 (2002), doi:10.1088/0953-8984/14/21/308.

[160] T. M. Hardy, J. P. Hague, J. H. Samson and A. S. Alexandrov, Superconductivity in a hubbard-fröhlich model and in cuprates, Phys. Rev. B **79**, 212501 (2009), doi:10.1103/PhysRevB.79.212501.

[161] N. Syassen, D. M. Bauer, M. Lettner, T. Volz, D. Dietze, J. J. Garcia-Ripoll, J. I. Cirac, G. Rempe and S. Dürr, Strong dissipation inhibits losses and induces correlations in cold molecular gases, Science **320**(5881), 1329 (2008), doi:10.1126/science.1155309.

[162] I. de Vega, D. Alonso and P. Gaspard, Two-level system immersed in a photonic band-gap material: A non-markovian stochastic schrödinger-equation approach, Phys. Rev. A **71**, 023812 (2005), doi:10.1103/PhysRevA.71.023812.

[163] S. Shams Es-haghi and D. J. Gardner, A critical evaluation and modification of the padé–laplace method for deconvolution of viscoelastic spectra, Molecules **26**(16) (2021), doi:10.3390/molecules26164838.

[164] V. Link, K. Müller, R. G. Lena, K. Luoma, F. Damanet, W. T. Strunz and A. J. Daley, Non-markovian quantum dynamics in strongly coupled multimode cavities conditioned on continuous measurement, doi:10.48550/ARXIV.2112.09499 (2021).

[165] H. M. Wiseman and G. J. Milburn, Quantum Measurement and Control, Cambridge University Press, doi:10.1017/CBO9780511813948 (2009).

[166] B. C. Hall, Lie Groups, Lie Algebras, and Representations, Springer, ISBN 978-3-319-13467-3 (2015).

[167] S. Flannigan, The application of quantum simulation to topological and open many-body systems, dissertation, University of Strathclyde (2020).

A   Quantum Jumps

In the following, we sketch the main equations of the method presented in Ref. [100]. First, it is convenient to define an effective, non-hermitian Hamiltonian:

$$\hat{H}_{\text{eff}} \equiv \hat{H}_{\text{tot}} - \frac{i}{2} \sum_l \hat{D}_l^\dagger \hat{D}_l \, , \tag{19}$$

that allows us to rewrite the Lindblad equation Eq. (2) as:

$$\partial_t \hat{\rho} = -i(\hat{H}_{\text{eff}}\hat{\rho} - \hat{\rho}\hat{H}_{\text{eff}}^\dagger) + \sum_l \hat{D}_l \hat{\rho} \hat{D}_l^\dagger \, . \tag{20}$$

Working with pure states, a stochastic process $\mathcal{Q}$ is introduced so that the density matrix time-evolved by the Lindblad equation is obtained from averaging over many realizations:

$$\mathcal{E}[|\Psi(t)\rangle_{\text{q}} \langle\Psi(t)|_{\text{q}}] = \hat{\rho}(t) \, , \tag{21}$$

where $q \in \mathcal{Q}$ is a collection of pseudo-random numbers identifying a so-called trajectory. Thus, instead of constructing the density matrix, one computes observables for every trajectory and averages over them:

$$\langle\hat{O}\rangle(t) = \mathcal{E}[\langle\Psi(t)|_{\text{q}} \hat{O} |\Psi(t)\rangle_{\text{q}}] \, . \tag{22}$$

In Fig. 9, we give a sketch of the described unravelling and the random processes involved. In practice, typically $\sim 10^2 - 10^3$ trajectories are needed for getting converged observables.

For a trajectory specified by two uniform random numbers $q = (q_1(t), q_2(t))$ with $q_i(t) \in [0, 1]$, the algorithm to compute the time-evolution of $|\Psi(t)\rangle_{\text{q}}$ is shown in Fig. 9. The general idea is to expand the time-evolved state to first order, to decompose the change in its norm

$$||\Psi^{(1)}(t + \delta t)\rangle|^2 = 1 - p \approx 1 - \delta t \sum_l \langle\Psi(t)| \hat{D}_l^\dagger \hat{D}_l |\Psi(t)\rangle \equiv 1 - \sum_l p_l \, . \tag{23}$$

Then, the random number $q_1(t)$ is picked and compared to the overall norm change p to decide whether a jump has to happen. If a jump needs to occur, the second random number $q_2(t)$ is picked to choose the actual jump operator, according to the different jump probabilities $\delta t \langle\Psi(t)| \hat{D}_l^\dagger \hat{D}_l |\Psi(t)\rangle$.

If the algorithm described above is carried out for each trajectory q, averaging over the projectors yields:

$$\begin{aligned}
\hat{\rho}(t + \delta t) &= \mathcal{E}[|\Psi(t)\rangle_{\text{q}} \langle\Psi(t)|_{\text{q}}] \\
&= (1 - p) \frac{|\Psi^{(1)}(t + \delta t)\rangle}{\sqrt{1 - p}} \frac{\langle\Psi^{(1)}(t + \delta t)|}{\sqrt{1 - p}} + \sum_l \frac{p_l}{p} \frac{\hat{D}_l |\Psi(t)\rangle}{\sqrt{p_l/\delta t}} \frac{\langle\Psi(t)| \hat{D}_l^\dagger}{\sqrt{p_l/\delta t}} \\
&= \hat{\rho}(t) - i\delta t(\hat{H}_{\text{eff}}\hat{\rho} - \hat{\rho}\hat{H}_{\text{eff}}^\dagger) + \delta t \sum_l \hat{D}_l \hat{\rho} \hat{D}_l^\dagger \, ,
\end{aligned} \tag{24}$$

which in the limit $\delta t \to 0$ is precisely the Lindblad equation.

$$|\Psi(t)\rangle \hookleftarrow \frac{1}{\sqrt{p_{l'}}}\hat{D}_{l'}|\Psi^{(1)}(t+\delta t)\rangle$$

| Time evolve $|\Psi^{(1)}(t+\delta t)\rangle = e^{-i\hat{H}_{\text{eff}}\delta t}|\Psi(t)\rangle$ | Choose l' with $q_2(t) \in [\tilde{p}_{l'-1}, \tilde{p}_{l'}]$ |

| Compute $\||\Psi^{(1)}(t+\delta t)\rangle|^2 = 1-p$ | Draw random number $q_2(t)$ |

| Draw random number $q_1(t)$ | Sort $\left\{\tilde{p}_l = \frac{p_l}{\sum_l p_l}\right\}_l$ in ascending order |

Yes

$|\Psi(t)\rangle \hookleftarrow |\Psi^{(1)}(t+\delta t)\rangle$

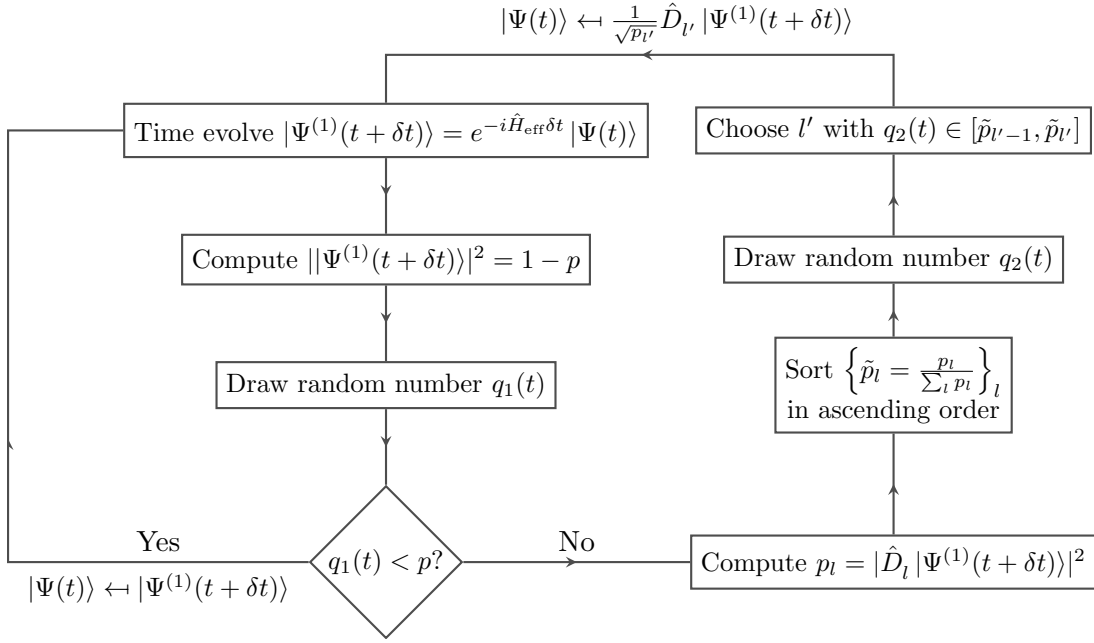$q_1(t) < p?$ No | Compute $p_l = |\hat{D}_l|\Psi^{(1)}(t+\delta t)\rangle|^2$ |

Figure 9: Algorithmic sketch of the quantum jumps method.

B   Hops

For clarity, we consider a single g, ω and κ. Tracing out the phonons transforms the Schrödinger equation with the Hamiltonian of Eq. (1) into the non-Markovian quantum state diffusion equation [102] for the state for the fermionic degrees of freedom $|\psi(t)\rangle$:

$$\partial_t |\psi(t)\rangle = -i\hat{H}_{\text{f}}|\psi(t)\rangle + g\sum_j \hat{L}_j z_j^*(t)|\psi(t)\rangle - g\sum_j \hat{L}_j^\dagger \int_0^t \mathrm{d}s\, \alpha_j^*(t-s)\frac{\delta|\psi(t)\rangle}{\delta z_j^*(s)}. \qquad (25)$$

Here $\alpha_j(t)$ represents the environment correlation function, which on site j and at zero temperature is given by the Fourier-transform of the spectral density $J_j(\omega)$. It can be determined, for instance, from spectroscopic experiments [1] :

$$\alpha_j(t) \equiv \langle\hat{a}_j(t)\hat{a}_j^\dagger(t')\rangle = \frac{1}{\sqrt{2}}\int_{-\infty}^{+\infty}\mathrm{d}\omega\, J_j(\omega)e^{-i\omega(t-t')} . \qquad (26)$$

In the following we assume that the environment correlation function is given by a single complex exponential $\alpha(t-t') = e^{-\kappa|t-t'|-i\omega(t-t')}$. The term $z_j(t)$ in Eq. (5) represents a colored noise that satisfies $\mathcal{E}[z_j(t)z_{j'}^*(t')] = \alpha(t-t')\delta_{j,j'}$, which can be generated in practice following e.g. [93, 162], while the term $\delta/\delta z_j^*(s)$ represents the functional derivative with respect to z^*. The observables for the electronic system are obtained by averaging the results of Eq. (5) over many trajectories, as explained for QJ in Sec. 2.1.

In practical calculations, solving Eq. (5) is exceptionally challenging because of the last term of the right-hand side, which is non-local in time [103]. This problem can be solved

---

[1] At finite temperature the relation between the environment correlation function and the spectral density reads: $\alpha(t) = \frac{1}{\pi}\int_0^\infty \mathrm{d}\omega\, J(\omega)\left[\coth\left(\frac{\beta\omega}{2}\right)\cos(\omega t) - i\sin(\omega t)\right]$
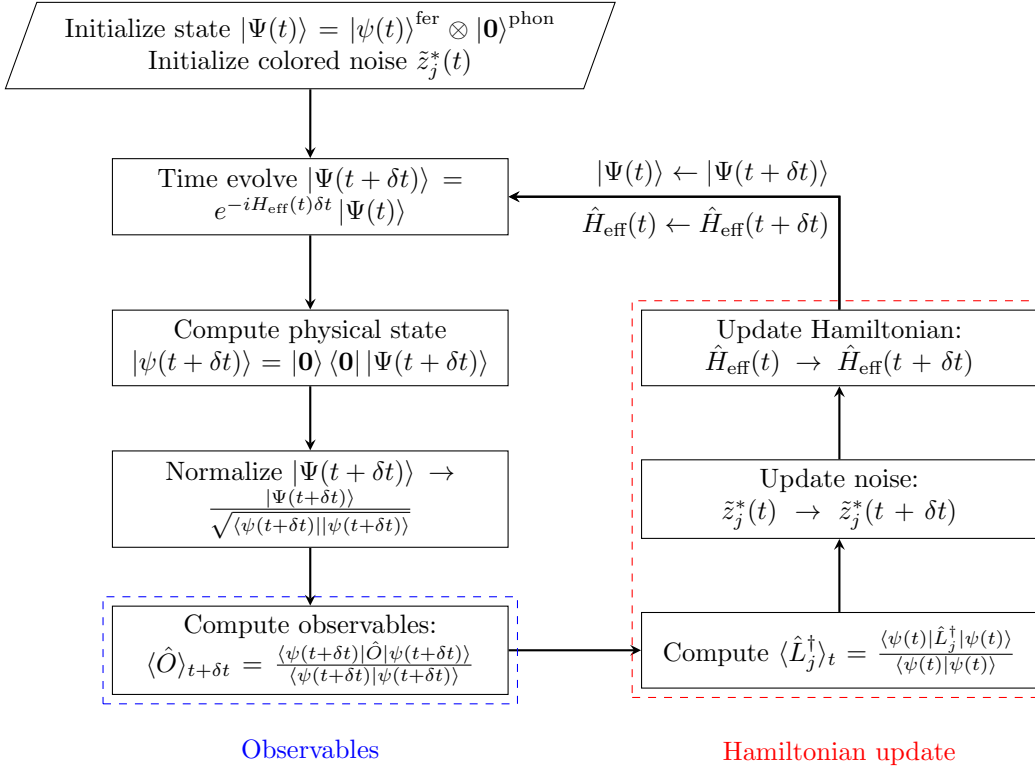
Figure 10: Algorithmic sketch of the hierarchy of pure states method.

efficiently by the hiearchy of pure states HOPS method [93,99], where one defines:

$$|\psi^{(1,j)}(t)\rangle = D_j(t) |\psi(t)\rangle \equiv \int_0^t \mathrm{d}s \, \alpha_j^*(t-s) \frac{\delta |\psi(t)\rangle}{\delta z_j^*(s)} \tag{27}$$

which is labelled *first auxiliary state* relative to site j. One then defines the *k-th auxiliary state* in a recursive manner:

$$|\psi^{(k,j)}(t)\rangle = [D_j(t)]^k |\psi(t)\rangle . \tag{28}$$

In Fig. 10 we sketch the HOPS algorithm. As discussed in App. B.1, at least for the model considered in this work, it is highly important to rescale the auxiliary states in the following way inspired by [94]:

$$|\psi^{(k,j)}(t)\rangle \rightarrow \frac{1}{\sqrt{\alpha_j(0)^k k!}} |\psi^{(k,j)}(t)\rangle . \tag{29}$$

With Eqs. (27) and (29), we can replace Eq. (5) by a hierarchy of equations. Following [93], it is convenient to define a state on the combined fermionic and bosonic Hilbert space as:

$$|\Psi(t)\rangle = \sum_{\mathbf{k}=1}^{k_{\max}} C_{\mathbf{k}}(t) |\psi^{(\mathbf{k})}(t)\rangle \otimes |\mathbf{k}\rangle^{\mathrm{bos}} , \tag{30}$$

where $|\mathbf{k}\rangle^{\mathrm{bos}} \equiv \otimes_j |k\rangle_j^{\mathrm{bos}}$ labels the bosonic mode corresponding to the k-th auxiliary state, $C_{\mathbf{k}}(t)$ is a time-dependent coefficient and $k_{\max}$ is the local bosonic Hilbert space dimension.

The hierarchy then takes the form of a simple Schrödinger equation for the state on the combined fermionic and bosonic Hilbert space:

$$\partial_t \left| \Psi(t) \right\rangle = -i \hat{H}_{\text{eff}}^{\text{Q}} \left| \Psi(t) \right\rangle \ , \tag{31}$$

where the effective, non-hermitian Hamiltonian now reads [93, 99]:

$$\hat{H}_{\text{eff}} = \hat{H}_{\text{s}} + \sum_j i \Big(\tilde{z}_j^*(t) g \hat{L}_j - (\kappa + i\omega) \hat{K}_j + g \hat{L}_j \otimes \hat{K}_j^{1/2} \hat{b}_j^\dagger - g \big(\hat{L}_j^\dagger - \langle \hat{L}_j^\dagger \rangle_t \big) \otimes \hat{b}_j \hat{K}_j^{1/2} \Big) \ . \tag{32}$$

Here, $\hat{K}_j$ is the bosonic number operator acting on site j and $\hat{b}_j^\dagger$, $\hat{b}_j$ are the so-called bare creation and annihilation operator, respectively, acting on the bosonic modes as:

$$\begin{aligned} \hat{b}^\dagger \left| k \right\rangle &= \left| k+1 \right\rangle \\ \hat{b} \left| k \right\rangle &= \left| k-1 \right\rangle \ . \end{aligned} \tag{33}$$

The colored noise is modified as:

$$\tilde{z}_j^*(t) = z_j^*(t) + g \int_0^t \mathrm{d}s \, \alpha_j^*(t-s) \langle \hat{L}_j^\dagger \rangle_s \ .$$

Eq. (31) is linearized by computing the non-linear term $\langle \hat{L}_j^\dagger \rangle_t$ with $\left| \psi(t - \delta t) \right\rangle$, which is a reasonable approximation as long as the timestep δt is small. For computing the electronic observables, at each timestep, the whole state needs to be projected onto the physical state:

$$\left| \Psi(t) \right\rangle \to \left| \psi(t) \right\rangle = \left| \mathbf{0} \right\rangle^{\text{bos}} \left\langle \mathbf{0} \right|^{\text{bos}} \left| \Psi(t) \right\rangle , \tag{34}$$

where $\left| \mathbf{0} \right\rangle^{\text{bos}} \equiv \otimes_j \left| 0 \right\rangle_j^{\text{bos}}$ is the bosonic vacuum. In practice, the Schrödinger equation Eq. (31) is propagated in time by using the initial condition $\left| \Psi(t=0) \right\rangle = \left| \psi^{(\mathbf{0})}(t=0) \right\rangle \otimes \left| \mathbf{0} \right\rangle^{\text{bos}}$, where all the auxiliary states are set to zero and are then populated as time evolves. In principle, $k_{\max}$ is infinite, but the populations of high-k auxiliary states typically remains small, allowing for a truncation of the hierarchy. In Sec. 2.3 and App. C.2 we will discuss how the newly-introduced PP method allows for an optimal and automated selection of $k_{\max}$.

The restriction of the environment correlation function $\alpha(t)$ being a complex exponential can be lifted by noting that complex exponentials form a complete orthonormal set on L^2, and thus we can approximate

$$\alpha_j(t - t') \approx \sum_{p=1}^P g_p e^{-\kappa_p |t-t'| - i\omega_p (t-t')} \ , \tag{35}$$

for any square-integrable function with arbitrary precision by increasing P. The decomposition can be obtained, for instance, with the Laplace-Pade method [163], yielding a set of parameters ω_p, g_p and κ_p. In this work, we will deal with the case $P = 1$, corresponding to the case of a Lorentzian spectral density. For a presentation of the conceptually straightforward generalization to $P > 1$ we refer to Ref. [94, 103].
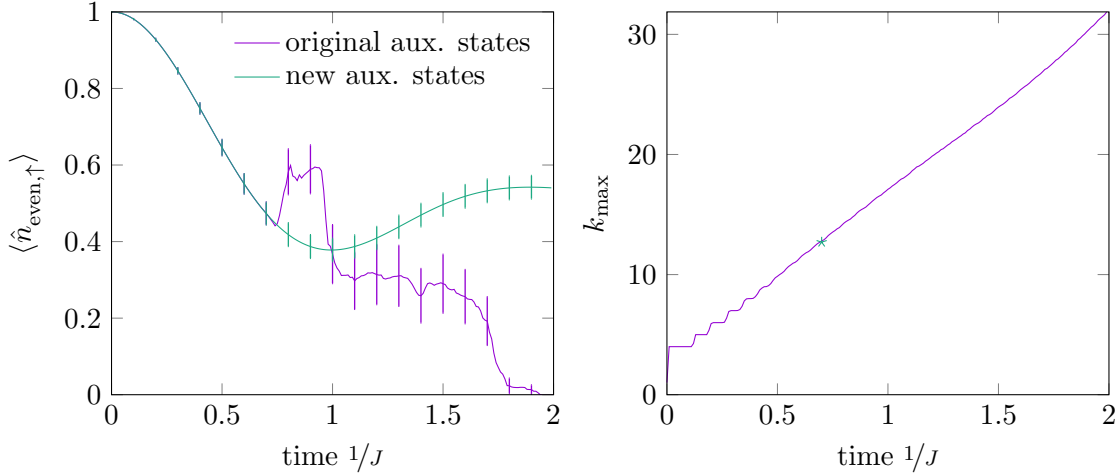
Figure 11: Improved stability of HOPS with auxiliary states transformed according to Eq. (29). Many phononic modes get populated in the strongly non-Markovian regime (right figure). With the original HOPS formulation, in such a case, the norm of the auxiliary states becomes very large and renders the method very unstable when computing observables with the normalized physical state (left figure). The calculations were performed for 20 sites and averaged over 100 trajectories with $g = J$ and $\kappa = 0.1\,J$. All other parameters are analog to Figs. 13 and 14.

B.1 Improved stability for highly excited baths

For all the HOPS calculations on the dissipative Hubbard-Holstein model, we have rescaled the auxiliary states according to Eq. (29). This reduces the norm of the auxiliary states and prevents numerical errors arising from the normalization of the physical state that is performed at each time step when computing the observables. In Fig. 11 we see that for a strong electron-phonon coupling $g = 1$, and a weak dissipation $\kappa = 0.1$, the HOPS method without a rescaling of the auxiliary states breaks down completely when 13 bosonic modes are populated. In contrast, as shown in Fig. 15, with the new definition of the auxiliary states HOPS can deal with up to 55 occupied bosonic modes. We want to point out that this is not an MPS-related issue, as we encountered it also for exact diagonalization (ED) calculations.

C   Method Benchmarks

Simulating the complicated interplay between electronic and dissipative, phononic degrees of freedom requires a careful understanding of the limitations of the used methods. Even though HOPS, as well as QJ, are well-established tools for the description of open quantum systems, here we combine these methods with a tensor-network representation that comes along with its own approximations. Additionally, we must consider the truncation in the enlarged phononic Hilbert space generated by the PP mapping Sec. 2.3. It is therefore essential to understand the effect of the additional numerical approximations, particularly if we can control the numerical precision within each method by tuning typical control parameters such as the bond dimension or the discarded weight [23, 40]. A practical consequence of the method benchmark presented
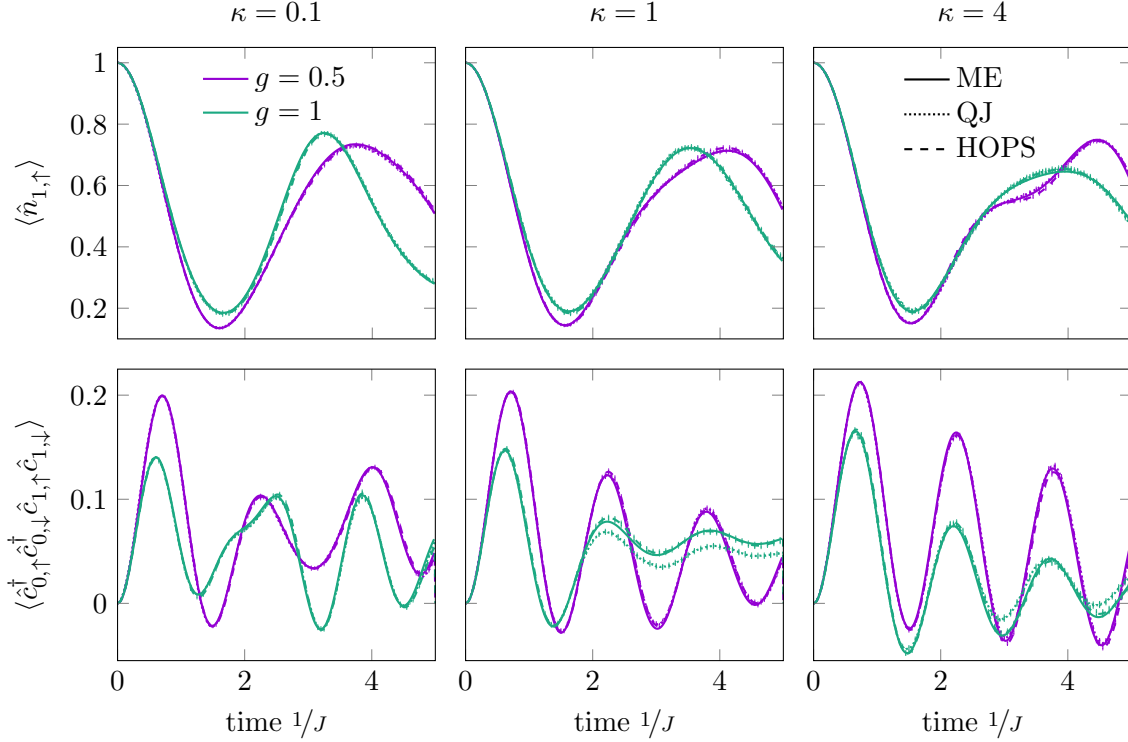
Figure 12: Comparing HOPS and QJ to the exact master equation (ME). All ME results were computed with ED for a system composed of two fermionic and two phononic sites. For all plots, the Hamiltonian parameters were chosen to be $U = J$, $\omega = 2\,J$, and 500 trajectories and a time step $dt = 0.005\,J^{-1}$ were used. The dissipation strength κ was fixed to $0.1\,J$ for the two upper plots and to $4\,J$ for the two lower plots. For all analyzed parameters, the linear and the non-linear method present at most very small differences. Both HOPS and QJ agree very well with the exact ME results, except for the case of intermediate and strong dissipation and large electron-phonon coupling ($\kappa = 1, 4\,J$, $g = J$) where QJ exhibits deviations at later times $t > 2\,J^{-1}$.

in the following is that even though both methods require similar numerical resources, their numerical accuracies complement each other with respect to the dissipation strength and electron-phonon coupling. Therefore, given a physical realization of some model parameters, our benchmark yields a comprehensive picture of which method is to be used for an optimal numerical outcome.

C.1 Exact diagonalization and matrix-product states

Analyzing the ground state of Eq. (11) already makes for a numerically involved problem. Thus, faithfully simulating the dynamics following a global quantum quench in the presence of dissipation, we are equipped with a reasonable benchmark system. Here, we prepare the system in a product state between the electronic and phononic system corresponding to a highly excited state of Eq. (11). As a key feature, in the post-quench dynamics, a potentially significant occupation of the bosonic, local degrees of freedom can occur, driven by the excess energy of the electronic system. The latter competes with the effect of dissipa-

tion. Considering large phonon frequencies $\omega \sim \mathcal{O}(1)$, the relaxation separates into distinct time-scales. Therefore, describing the dynamics of the overall system requires a large local Hilbert space dimension $\sim 10 - 60$ for the bosonic system. Capturing these competing effects correctly is one of the most important points in practice, whereas any small, uncontrolled approximation already modifies the short-time dynamics of correlation functions drastically. Note that quenching from a product state, a large amount of energy is transferred into the system. In that sense, our analysis refers to an extreme test case. In practice, for near-equilibrium quenches, we expect both methods to perform reasonably also in the regime, which is complementary to the optimal one described in the following.

Comparison with exact diagonalization. The dynamics of the smallest meaningful Hubbard-Holstein model, composed of two electrons and two phonons, can be described by the exact Lindblad master equation (Eq. (2)) via ED. [2]This is used as an exact reference to assess the precision and the computational complexity of the HOPS and the QJ methods before turning to large systems. We fix $U = J$ and $\omega = 2\,J$, and study the performance of the HOPS and the QJ methods as a function of the electron-phonon coupling g and the dissipation strength κ. The dependence on the dissipation strength is particularly interesting because, in principle, the two methods are complementary: for HOPS, the environment becomes Markovian and thus trivial for $\kappa \to \infty$, whereas for QJ, the non-unitary part of the dynamics for the enlarged system becomes irrelevant in the limit $\kappa \to 0$. We initialize the time-evolution with the Neel state for the fermions and the vacuum for the phonons:

$$|\Psi\rangle^{\mathrm{init}} = |\uparrow\rangle_1^{\mathrm{fer}} |\downarrow\rangle_2^{\mathrm{fer}} |0\rangle_1^{\mathrm{bos}} |0\rangle_2^{\mathrm{bos}}$$

and perform a global quench both in the electronic and in the phononic system. We pick the number of spin-up fermions on site one: $\langle \hat{n}_1^\uparrow \rangle$, and the pairing correlation between the two fermionic sites: $\langle \hat{c}_{0,\uparrow}^\dagger \hat{c}_{0,\downarrow}^\dagger \hat{c}_{1,\downarrow} \hat{c}_{1,\uparrow} \rangle$, as a single-site and two-site observable, respectively. We choose to compare the two methods for very weak ($\kappa = 0.1\,J$), intermediate ($\kappa = J$) and very strong ($\kappa = 4\,J$) dissipation at the medium and strong electron-phonon couplings $g = 0.5\,J$ and $g = J$.

Our results are summarized in Fig. 12. In general we observe excellent agreement for both HOPS and QJ with ME at short times $t \leq 2\,J^{-1}$. The only notable deviation appears at larger simulation times in the QJ results for the two-site observable, in the case of strong electron-phonon coupling $g = 1J$ and medium or strong dissipation $\kappa \geq 1J$. We believe that using a modified version of QJ, or significantly decreasing the timestep and increasing the number of trajectories, would improve the agreement with the exact result. However, with MPS methods, using an excessively small timestep can lead to an accumulation of truncation errors and should be avoided. Therefore, we suggest that, at least for a quench from a product state, HOPS should be preferred over QJ in the parameter regime mentioned above. In App. D, we show that both the linear and the non-linear version of the homodyne detection unravelling do not yield accurate results for this model.

---

[2]Note that due to the large local Hilbert space dimension required for the phonons, already the exact treatment of the two-electron + two phonon-case is non-trivial. For instance, the total Hilbert space dimension for the density matrix for two electrons and two phonons modelled by a 10-level harmonic oscillator is $\sim 2.6\cdot10^6$. For some MPS calculation, we included up to 60 phononic states, which would correspond to a total Hilbert space dimension of $\sim 3.3 \cdot 10^9$ for a two-site system.
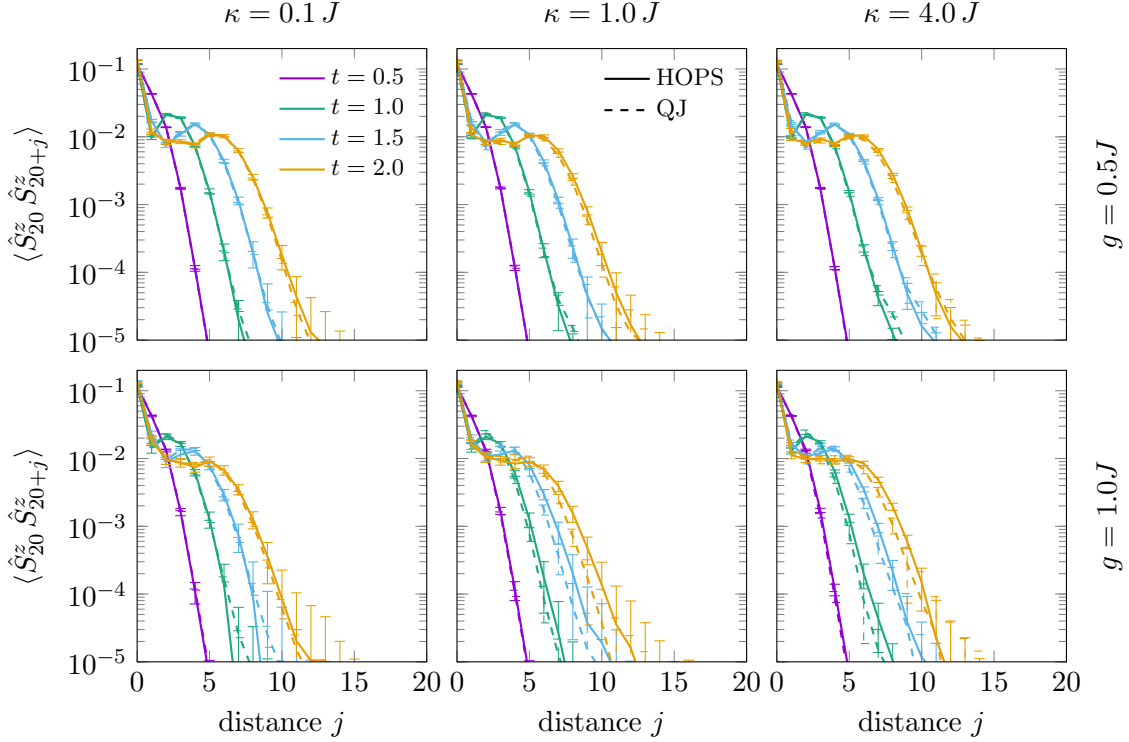
Figure 13: Spin-density correlations $\langle \hat{S}^z_{20} \hat{S}^z_{20+j} \rangle$ calculated using HOPS and QJ for a system with $L = 40$ sites at half-filling, quenched from a Neel state with two different values of g (columns) and three different values of κ (rows). The two methods agree very well, even for long-range correlations. Only small deviations between HOPS and QJ are found for large electron-phonon coupling $g = J$ and intermediate and strong dissipation $\kappa = 1\,J, 4\,J$. We chose a timestep $\delta t = 0.005\,J^{-1}$ for QJ and $\delta t = 0.01\,J^{-1}$ for HOPS, since the latter method has shown to be less sensitive on the timestep.

Comparison beyond exact diagonalization. We proceed with the comparison by considering the same parameters as in Fig. 12 but increase the system size to $L = 40$. Such system sizes are far beyond reach for ED methods, as well as density operator based time-evolution schemes, in particular when considering a large number of phononic modes (here ≤ 40) per site, too. In order to ensure numerical convergence, throughout the benchmark calculations, we varied all relevant parameters. Table 1 displays the settings we found to produce faithful and converged results. In particular, we fix the maximally allowed bond dimension to $m_{\max} = 6000$ and choose a time step $\delta t = 0.01\,J^{-1}$ for HOPS and $\delta t = 0.005\,J^{-1}$ for QJ and a discarded weight of $\delta = 10^{-10}$. The maximally allowed hierarchy depth $k_{\max}$ (for HOPS) and local Hilbert space dimension of the phonons $b_{\max}$ (for QJ) are set to $k_{\max} = b_{\max} = 40$. We find that these values are sufficient to describe the dynamics, and correspondingly, the actually exploited local dimensions never reach their respective upper limit. Since the initial state is a product state, we start the time-evolution with the global Krylov method and then switch to the two-site time-dependent variational principle (2TDVP) method. Here, at least ~ 50 Krylov time-evolution steps with otherwise identical numerical configuration are required in order to obtain converged results.
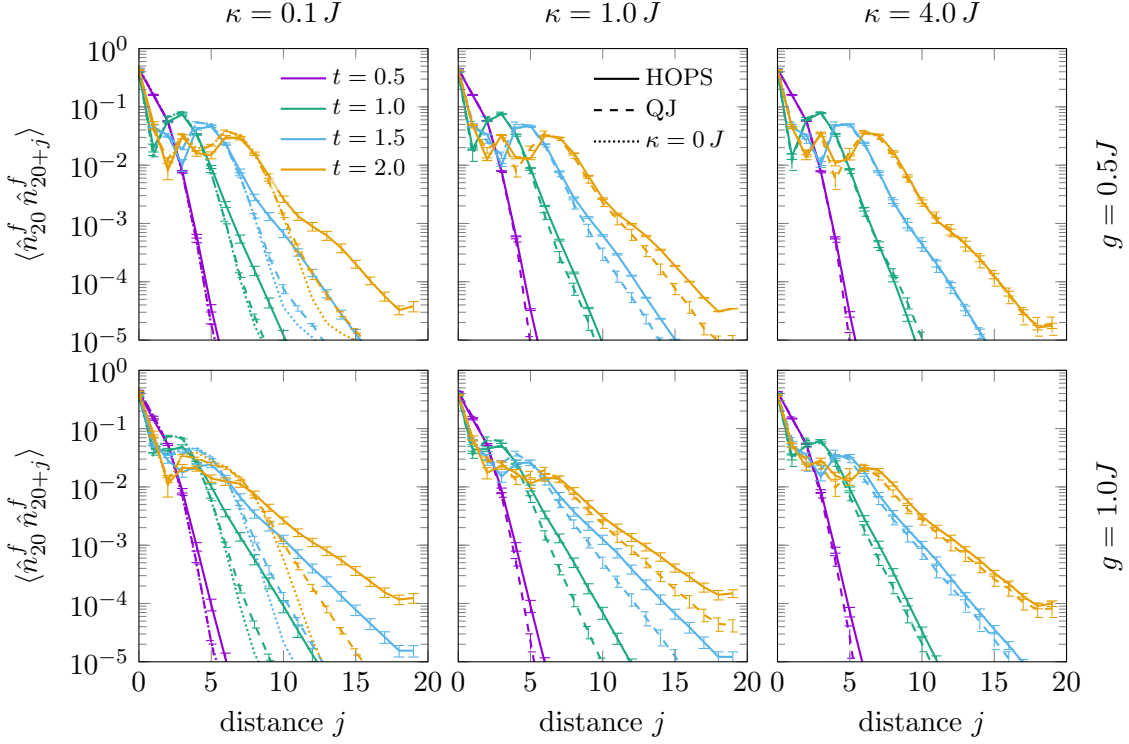
Figure 14: Charge-density correlations $\langle \hat{n}_{20}^f \hat{n}_{20+j}^f \rangle$ calculated with HOPS and QJ for the same quench as the one in Fig. 13. A disagreement is observed at later times and long distances. In the upper-left panel, at each time, we have added a dotted line that represents the case without dissipation, i.e. a simple Schrödinger evolution with the Hubbard-Holstein Hamiltonian. This indicates that the long-range correlations in case of very weak dissipation are better described by QJ than by HOPS.

Our comparisons aim to determine the model parameter regimes in which QJ and HOPS are capable of describing the many-body post-quench dynamics. Since the dynamics are characterized by the spreading of correlations on different time scales, in the following, we concentrate on our results for the dynamics of spin-density and charge-density correlation functions w.r.t. the central site. However, we note that during our investigations, both methods performed equally well when describing on-site observables. As shown in Fig. 13, the spin-density correlations agree very well for the two methods. However, for the charge-density correlations displayed in Fig. 14 we find deviations in the long-distance behavior for very weak dissipation. An additional shoulder characterizes them in the tail of the correlation functions at times $t > 1\,J^{-1}$, occurring in the dynamics obtained from HOPS. This shoulder corresponds to an increased spreading of density correlations in the HOPS result, compared to QJ [3]. In order to clarify which method yields more reliable results in this regime, we performed a comparison to the quench dynamics in the absence of dissipation. As shown in the upper-left panel of Fig. 14 by the dotted curves, we find that QJ smoothly connects to the non-dissipative case. We take this observation as an indicator that QJ is more precise in the case of small dissipation strengths.

---

[3]We have checked that halving the timestep of HOPS does not improve the results.

	d-surface Figs. 15 and 16	QJ and HOPS Figs. 13, 14 and 17	double occupations Fig. 5b	bipolaron metallicity Figs. 6 and 7
δ	10^{-10}	10^{-10}	10^{-10}	10^{-10}
$m_{\max}$	6000	6000	500	2000
$d_{\max}$	60	40	40	40
sites	10	40	20	20
$|\mathcal{Q}|$	5	200	50	200

Table 1: Summary of the most relevant simulation parameters: the max. allowed discarded weight δ, the max. allowed MPS bond dimension $m_{\max}$, the max. allowed local dimension $d_{\max}$, and the overall number of trajectories $|\mathcal{Q}|$.
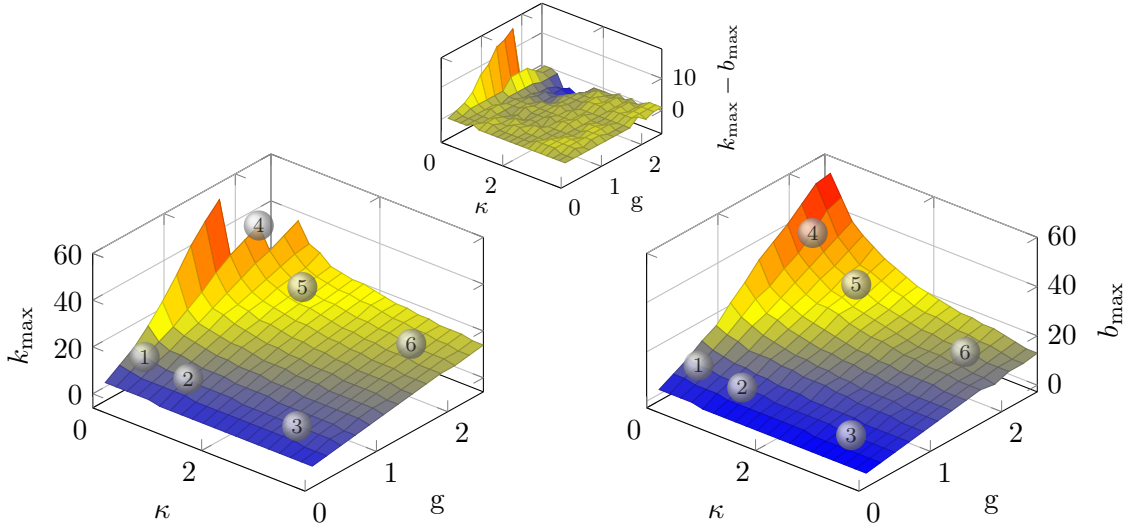

Figure 15: Left: hierarchy dept $k_{\max}$ for HOPS as a function of g and κ. Right: local physical dimension of the phonons $b_{\max}$ for QJ g and κ. Center: difference between $k_{\max}$ and $b_{\max}$. The truncation is determined automatically via the PP method by fixing a discarded weight $\delta = 10^{-10}$. For all calculations, the model parameters were $N_{\text{sites}} = 10$, $U = J$, and $\omega = 2\,J$ and time-evolution has been performed until $T_{\max} = 2\,J^{-1}$. We computed 10 trajectories for each point. For the six points marked by a sphere, a convergence analysis of an observable is described in Fig. 16 and in the main text. Note that at very large g and very small κ (i.e., the scattered top left area in the left figure), HOPS collapses, a finding which we discuss in the main text.

C.2   Numerical complexity and stability

From a practical point of view, it is important to clarify if the methods are numerically feasible in the identified optimal parameter regimes. Here, we start by comparing the hierarchy depth $k_{\max} \equiv d_{\max}$ for HOPS with the local Hilbert space dimension of the phonons $b_{\max} \equiv d_{\max}$ for QJ for different values of g and κ. Using 2TDVP as time-evolution method, the numerically most costly operations scale as $\mathcal{O}(m_{\max}^3 d_{\max}^2 \delta_{\max})$ and $\mathcal{O}(m_{\max}^2 d_{\max}^3 \delta_{\max}^2)$. In case of considerably large local dimensions $d_{\max} > 10$, the latter operations become dominant and

the applicability of QJ and HOPS depends on their required local Hilbert space dimensions.

In Fig. 15 we show the evolution of $d_{\max} = k_{\max}, b_{\max}$ required to ensure an overall discarded weight $\delta = 10^{-10}$ throughout the time-evolution. Note that the PP-truncation scheme generically truncates the required local dimension so that the shown results already constitute the optimal number of local basis states that need to be kept. Interestingly, we find that despite being conceptually very different, each method's required local Hilbert space dimensions $k_{\max}$ (left plot) and $b_{\max}$ (right plot), display a strikingly similar dependence on g and κ, throughout the whole analyzed parameter space. A broad connection between these two quantities is discussed for another model in Ref. [164]. The shape of the surfaces drawn by $k_{\max}$ and $b_{\max}$ confirms our previous observation that in the case of strong electron-phonon coupling and weak dissipation, many highly-excited phononic modes are populated that can not escape due to dissipation, and thus large Hilbert space dimensions are required. Note that for HOPS the top-left corner of the $k_{\max}$ surface is missing. This is due to the fact that for a few extreme cases of very strong electron-phonon coupling and very weak dissipation, HOPS becomes numerically unstable because the norm of the auxiliary states grows very large. In App. B.1 we show that, at least for the dissipative Hubbard-Holstein model, this instability for the HOPS method is much more severe when the original definition of the auxiliary states is adopted instead of the modified one of Eq. (29). We thus find that the numerical costs are equivalent for both methods when enforcing a certain discarded weight.

When performing a time-evolution, one is typically interested in the convergence of some specific observables and not in the approximation quality of the wave function controlled by the discarded weight. Therefore, we pick six representative parameter points marked by circles in Fig. 15 and studied the convergence of the nearest-neighbor pairing correlation function:

$$C_{nn}^{pa,d_{\max}} = \frac{1}{L-1} \sum_{j=1}^{L-1} \langle \hat{c}_{j,\uparrow}^\dagger \, \hat{c}_{j,\downarrow}^\dagger \, \hat{c}_{j+1,\downarrow} \, \hat{c}_{j+1,\uparrow} \rangle \ . \tag{36}$$

We calculated its dependency on the maximally allowed local dimension, compared to a reference value $\hat{C}_{nn}^{pa,k_{\max}}$ which was obtained fixing the discarded weight only and using the values of $k_{\max}, b_{\max}$ extracted from Fig. 15:

$$\mathrm{Err}(j) = \left| \left(C_{nn}^{pa,d_{\max}} - C_{nn}^{pa,d_{\max}j} \right) / C_{nn}^{pa,d_{\max}} \right| \ . \tag{37}$$

Here, for both methods, we varied $j \in \{1/4, 1/2, 3/4\}$, reducing the maximally allowed local dimension up to a quarter of the optimal value. In Fig. 16, we show the obtained convergence for the different fractions j indicated by the different line styles. We observe that most of the time, the HOPS curves lay below the QJ curves, i.e., they exhibit less sensitivity on truncating the local Hilbert space dimension. Noting that in HOPS, the bosonic degrees of freedom represent auxiliary states with no direct physical meaning, it is reasonable to expect it to be somewhat less sensitive on truncations in the bosonic Hilbert space than QJ.

Aside from the local dimension, we also analyzed the bond dimension $m_{\max}$, which is of particular importance when using the PP mapping, as it also controls the approximation quality of the phonon 1RDMs (c.f. Sec. 2.3). The results are displayed in Fig. 17 for the same model parameters as for the benchmark calculation shown in Figs. 13 and 14. Similarly to the local dimensions, the required bond dimensions decrease when the dissipation strength increases. Notably, we find that for all six analyzed (g, κ), QJ features a smaller bond dimension than HOPS when enforcing a constant discarded weight. We investigated
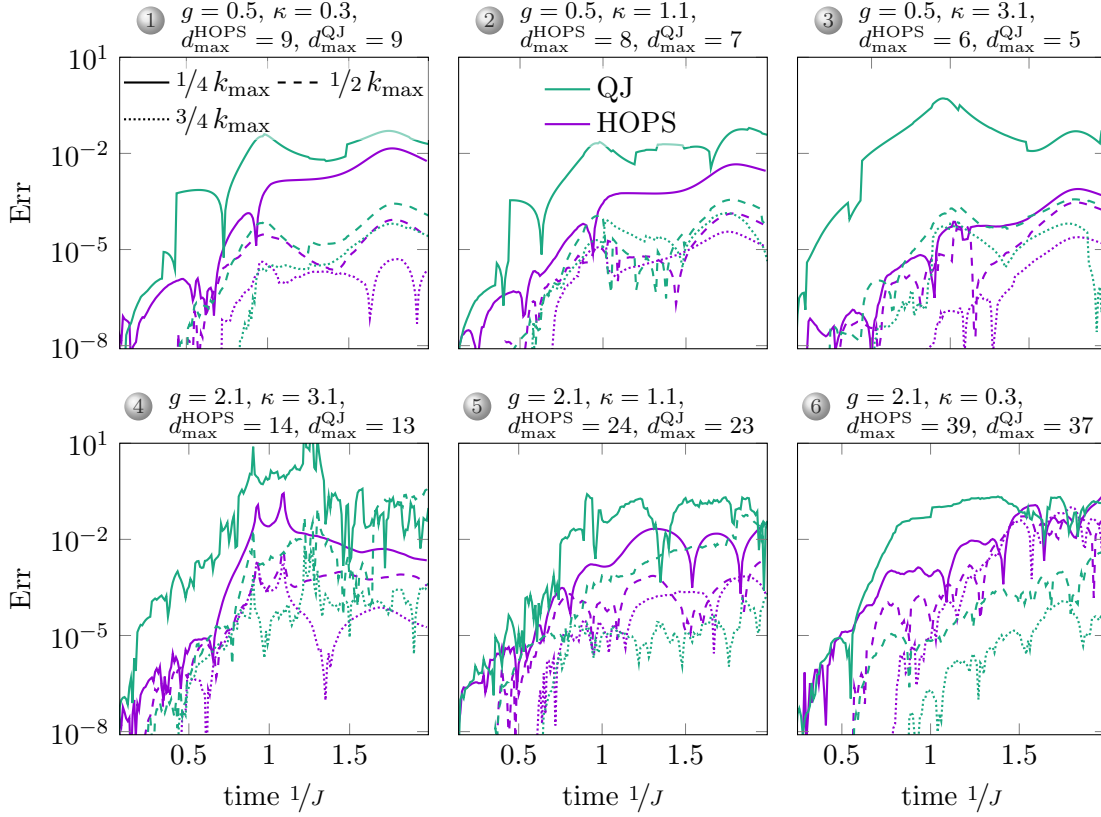
Figure 16: Convergence of nearest neighbor pairing correlation Eq. (36) in the local Hilbert space dimension $jd_{\max}$. The chosen six parameter sets (g, κ) are indicated in Fig. 15. At each time step, the relative error between a reference time evolution performed with the optimal local dimension $d_{\max}$ is evaluated. All the model and time evolution parameters are analog to Fig. 15. Note that more than one trajectory is used only to avoid the risk of picking a particularly favorable or unfavorable combination of random numbers, but the error analysis here is not concerned with the statistical averaging performed for pure state methods.
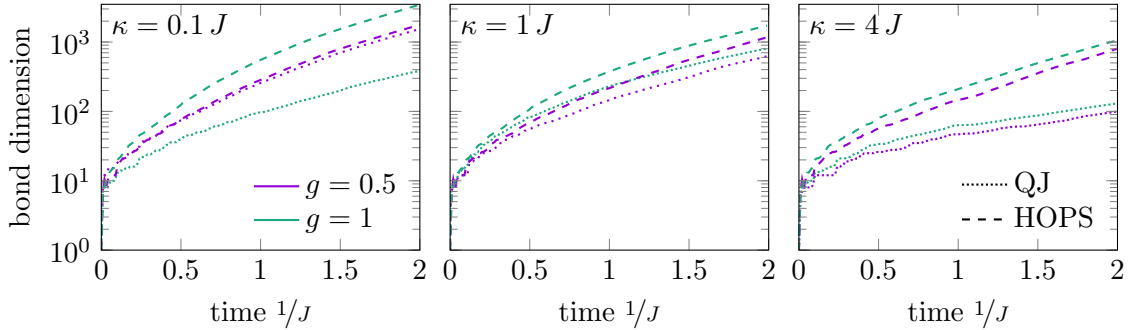

Figure 17: Bond dimension for QJ and HOPS during time evolution after the global quenches, specified in the caption of Fig. 13.

the possible origins of this surprising observation. One possible reason may be buried in the

fact that whenever a jump occurs, e.g., an annihilator is applied on a phononic site, the bond dimension drops significantly because a large portion of the local Hilbert space is projected out. Moreover, it has been shown recently that repeated measurements reduce the support of lattice sites, on which correlations can spread significantly [42, 140] and thereby also reduce entanglement growth. Since in QJ the probability for a jump to happen is mainly controlled by the dissipation strength, we would expect considerably smaller bond dimensions to happen if κ is large, as observed in the right panel of Fig. 17. Furthermore, for small dissipation strengths and large electron-phonon interactions, we also observed a significant increase in the required local dimension of HOPS. Since in the PP mapping, the required local dimension is directly connected to the decay of the phonon 1RDM diagonal elements, HOPS seems to have the tendency to create more substantial fluctuations in the phonon system in this parameter regime and thereby increases the overall bond dimension. However, deciding whether the overall trend displayed in Fig. 17 is a peculiar feature of the analyzed systems or a general feature is beyond the scope of this work.

D   Quantum State Diffusion

D.1   Linear and non-linear homodyne detection

An alternative unraveling of the Lindblad master equation Eq. (2) is given by the so-called linear homodyne detection (lHD) [69]. Similarly to HOPS, the stochastic part is represented by a random noise term contained in the effective Hamiltonian. For each trajectory $\mathcal{Q}$, the time-evolution is generated by the non-hermitian Hamiltonian ([165]) :

$$\hat{H}_{\mathrm{eff}}^{\mathrm{Q}} = \hat{H}_{\mathrm{s}} + i \sum_l \left[Z_l(t)\hat{D}_l - \frac{C_l}{2}\hat{D}_l^\dagger \hat{D}_l \right] , \tag{38}$$

where $\hat{H}_{\mathrm{s}}$ is the system Hamiltonian, $\hat{D}_l$ are the Lindblad operators, and $Z_l(t)$ is a random number drawn from a real-valued Gaussian distribution with mean zero and standard deviation σ given by the square root of the coupling parameter C_l divided by the time step δt. To show the equivalence between the Lindblad evolution and lHD method, we time-evolve a state $|\Psi(t)\rangle$ to first order with the effective Hamiltonian of Eq. (38), considering the case of only one Lindblad operator for clarity:

$$|\Psi(t + \delta t)\rangle = \left[1 + \delta t\left(-i\hat{H}_s + \hat{D}Z(t) - \frac{C}{2}\hat{D}^\dagger \hat{D}\right)\right] |\Psi(t)\rangle . \tag{39}$$

To first order in δt (recalling that Z^2 is $\mathcal{O}(\delta t^{-1})$), the outer product of Eq. (39) with its hermitian conjugate reads:

$$\begin{aligned}|\Psi(t + \delta t)\rangle \langle\Psi(t + \delta t)| = &|\Psi(t)\rangle \langle\Psi(t)| + \delta t\left(-i\hat{H}_s + \hat{D}Z(t) - \frac{C}{2}\hat{D}^\dagger \hat{D}\right) |\Psi(t)\rangle \langle\Psi(t)| \\ &+ |\Psi(t)\rangle \langle\Psi(t)| \delta t\left(+i\hat{H}_s + \hat{D}^\dagger Z(t) - \frac{C}{2}\hat{D}^\dagger \hat{D}\right) \\ &+ \delta t^2 Z^2(t)\hat{D} |\Psi(t)\rangle \langle\Psi(t)| \hat{D}^\dagger .\end{aligned}$$
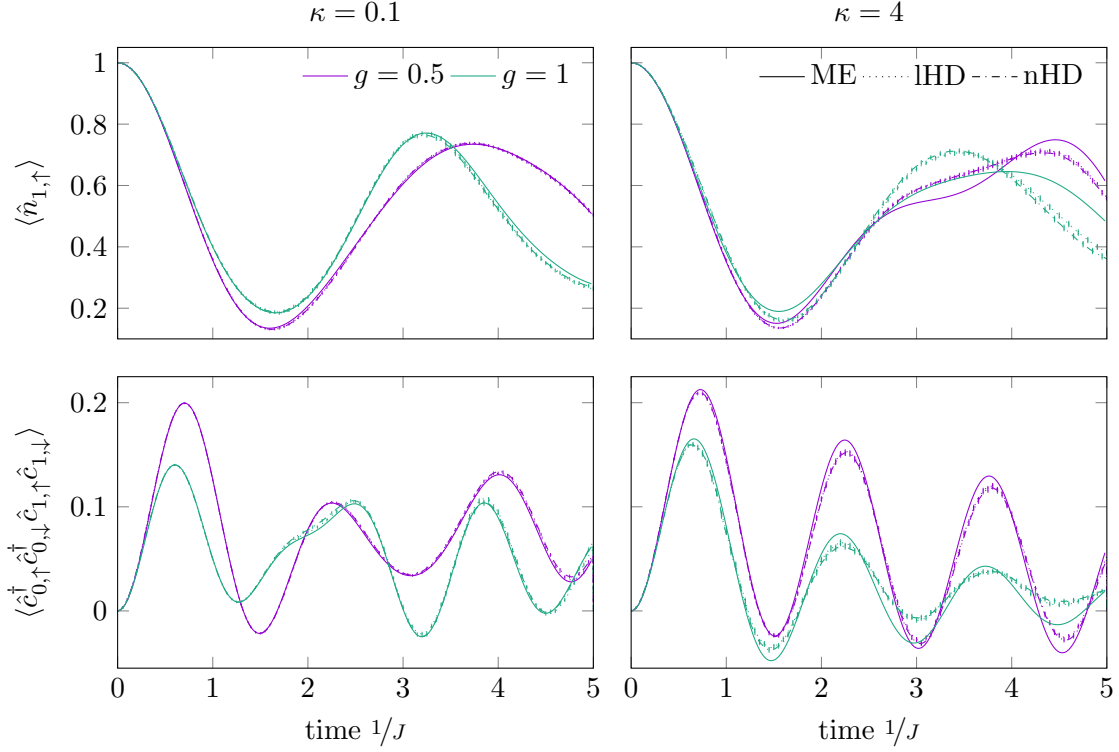
Figure 18: Comparing the linear and non-linear homodyne detection to the exact ME. All results were computed with ED for a system composed of two fermionic and two phononic sites. For all plots, the Hamiltonian parameters were chosen to be $U = J$, $\omega = 2\,J$, and 500 trajectories and a time step $dt = 0.005\,J^{-1}$ were used. The dissipation strength κ was fixed to $\kappa = 0.1\,J$ for the two upper plots and to $\kappa = 4\,J$ for the two lower plots. For all analyzed parameters, the linear and the non-linear method present at most very small differences. While both methods agree reasonably well with the exact results for a small dissipation strength, for strong dissipation, the homodyne detection results deviate strongly from the exact ones, and the problem becomes more severe for large electron-phonon coupling.

Now, by making use of the mean and the variance of Z, namely $\mathcal{E}[Z(t)] = 0$ and $\mathcal{E}[Z^2(t)] = C/\delta t$ we compute the ensemble average over the projectors:

$$
\begin{aligned}
\mathcal{E}[|\Psi(t+\delta t)\rangle \langle\Psi(t+\delta t)|] \equiv \hat{\rho}(t+\delta t) &= \hat{\rho}(t) + \delta t(-i\hat{H}_s - \frac{C}{2}\hat{D}^\dagger\hat{D})\hat{\rho}(t) \\
&+ \hat{\rho}(t)\delta t(+i\hat{H}_s - \frac{C}{2}\hat{D}^\dagger\hat{D}) + \delta t^2\frac{C}{\delta t}\hat{D}\hat{\rho}(t)\hat{D}^\dagger \\
&= \hat{\rho}(t) + \delta t\big(-i[\hat{H}_s, \hat{\rho}(t)] - \frac{C}{2}\{\hat{D}^\dagger\hat{D}, \hat{\rho}(t)\} + C\hat{D}\hat{\rho}(t)\hat{D}^\dagger\big) ,
\end{aligned}
$$

which, in the limit $\delta t \to 0$, is the Lindblad equation. For the case of the dissipative Hubbard-Holstein model considered in App. C and Sec. 3, the effective Hamiltonian reads:

$$
\hat{H}_{\text{eff}}^{\text{Q}} = \hat{H}_{\text{HH}} + i\sum_{j=1}^{L}\big[Z_j(t)\hat{a}_j - \frac{\kappa}{2}\hat{a}_j^\dagger\hat{a}_j\big] , \tag{40}
$$

with the constant coupling being the dissipation strength κ.

In order to try to lower the number of trajectories needed to converge the observables for this pure-state method, a modification of Eq. (38) called non-linear homodyne detection (nlHD) can be used ([165]):

$$\hat{H}_{\text{eff}}^{\text{Q}} = \hat{H}_{\text{s}} + i \sum_{j=1}^{L} \left[Z_j(t)\hat{D}_j - \frac{C_j}{2}\hat{D}_j^\dagger \hat{D}_j + C_j \langle\Psi(t)| (\hat{D}_j^\dagger + \hat{D}_j) |\Psi(t)\rangle \hat{D}_j \right] . \tag{41}$$

Analogously to what is done for HOPS, the non-linear dynamics generated by Hamiltonian Eq. (41) are linearized by computing the expectation value with the state $|\Psi(t - \delta t)\rangle$, which is a reasonable approximation as long as the time step δ is small.

We show the ED comparison of both the linear and the non-linear homodyne detection methods to the ME methods for the same parameters used in Fig. 12. Figure 18 shows that lHD and nlHD work well for small dissipation but fail to yield correct results both for single-site and for two-site observables in the case of large dissipation. We thus conclude that the QJ method is more suitable to be used as a comparison to HOPS.

D.2 Exact factorization of the time-evolution operator

The matrix elements of the non-hermitian part of the effective Hamiltonian can be computed exactly, both for the linear and the non-linear case. Also, the MPO-representation of the phononic displacement operator used for the computation in Sec. 3 is obtained in a completely analogous way. We first consider the linear case Eq. (40), define $\hat{B} \equiv \sum_{j=1}^{L} \left[Z_l(t)\hat{a}_l - \frac{\kappa}{2}\hat{a}_l^\dagger \hat{a}_l \right]$ and start by factorizing the exponential of the effective Hamiltonian via a second-order Trotter decomposition:

$$e^{-i(\hat{H}_{\text{HH}}+i\hat{B})\delta t} \approx e^{\hat{B}\delta t/2} \cdot e^{-i\hat{H}_{\text{HH}}\delta t} \cdot e^{\hat{B}\delta t/2} + \mathcal{O}(\delta t^3). \tag{42}$$

We then focus on calculating the exponential $e^{B\delta t}$. Since the terms acting on each site commute, the expression

$$e^{\sum_{j=1}^{L} \left[Z_j(t)\hat{a}_j - \frac{\kappa}{2}\hat{a}_j^\dagger \hat{a}_j \right]\delta t} = e^{\left[Z_1(t)\hat{a}_1 - \frac{\kappa}{2}\hat{a}_1^\dagger \hat{a}_1 \right]\delta t} \cdot e^{\left[Z_2(t)\hat{a}_2 - \frac{\kappa}{2}\hat{a}_2^\dagger \hat{a}_2 \right]\delta t} \cdots e^{\left[Z_L(t)\hat{a}_L - \frac{\kappa}{2}\hat{a}_L^\dagger \hat{a}_L \right]\delta t}$$

is exact. We consider the expression for one site and drop the site subscript and the explicit time dependency of Z:

$$e^{\left[Z\hat{a} - \frac{\kappa}{2}\hat{a}^\dagger \hat{a} \right]\delta t} . \tag{43}$$

We now want to write this exponential as a product of two exponentials. We use the following theorem from Ref. [166]: Given two operators $\hat{X}$ and $\hat{Y}$, if $[\hat{X}, \hat{Y}] = s\hat{Y}$ with $s \in \mathbb{C}, s \neq 2\pi i n, n \in \mathbb{N}$, then $e^{\hat{X}} \cdot e^{\hat{Y}} = \exp\left\{ (\hat{X} + \frac{s}{1-e^{-s}}\hat{Y}) \right\}$. Applied to Eq. (43), this theorem implies that:

$$e^{\left[Z\hat{a} - \frac{\kappa}{2}\hat{a}^\dagger \hat{a} \right]\delta t} = e^{\left[-\frac{\kappa}{2}\hat{a}^\dagger \hat{a} + \frac{s}{1-e^{-s}}\tilde{Z}\hat{a} \right]\delta t} = e^{-\frac{\kappa}{2}\hat{a}^\dagger \hat{a}\delta t} \cdot e^{\tilde{Z}\hat{a}\delta t} , \tag{44}$$

with $\tilde{Z} = Z\frac{1-e^{-s}}{s}$, $s = \frac{\kappa}{2}\delta t$. Finally, the factorized operator reads:

$$e^{\left[Z\hat{a} - \frac{\kappa}{2}\hat{a}^\dagger \hat{a} \right]\delta t} = e^{-\frac{\kappa}{2}\hat{a}^\dagger \hat{a}\delta t} \cdot e^{Z\frac{1-e^{-\kappa\delta t/2}}{\kappa\delta t/2}\hat{a}\delta t} = e^{-\frac{\kappa}{2}\hat{a}^\dagger \hat{a}\delta t} \cdot e^{Z\frac{1-e^{-\kappa\delta t/2}}{\kappa/2}\hat{a}} . \tag{45}$$

The operator $e^{Z\frac{1-e^{-K\delta t/2}}{\kappa/2}\hat{a}}$ does not conserve the bosonic particle number. The $U(1)$ symmetry is restored in the PP mapping, by replacing the annihilator $\hat{a}$ with $\hat{a} \otimes \hat{b}^{\dagger}$, where $\hat{b}^{\dagger}$ is the balancing operator acting on the bath site. By defining the prefactor as $\gamma(Z)$ we get:

$$e^{-\frac{\kappa}{2}\hat{a}^{\dagger}\hat{a}\delta t} \cdot e^{\gamma(Z)\hat{a}\otimes\hat{b}^{\dagger}} \ .$$

We now want to calculate the MPO representation of the dissipative operator: We thus compute the matrix elements:

$$\langle n, n'| e^{-\frac{\kappa}{2}\hat{a}^{\dagger}\hat{a}\delta t} \cdot e^{\gamma(Z)\hat{a}\otimes\hat{b}^{\dagger}} |m, m'\rangle = e^{-\frac{\kappa}{2}n\delta t} \sum_{l=0}^{\infty} \frac{\gamma(z)^{l}}{l!} \langle n| \hat{a}^{l} |m\rangle \langle n'| (\hat{b}^{\dagger})^{l} |m'\rangle = \tag{46}$$

$$e^{-\frac{\kappa}{2}n\delta t} \sum_{l=0} \frac{\gamma(z)^{l}}{l!} \sqrt{\frac{(l+n)!}{n!}} \delta t_{n+l,m} \delta t_{n',m'+l} = \begin{cases} 0, & n > m \\ \frac{e^{-\frac{\kappa}{2}n\delta t}}{(m-n)!}\gamma(Z)^{m-n}\sqrt{\frac{m!}{n!}}\delta t_{n'-m',m-n}, & \text{otherwise.} \end{cases} \tag{47}$$

We can rewrite the rank 4-tensor $\delta t_{n'-m',m-n}$ as

$$\delta t_{n'-m',m-n} = \sum_{a=0}^{d-1} \delta t_{n'-m',a} \delta t_{m-n,a} \ .$$

Thus we get the expression:

$$e^{-\frac{\kappa}{2}\hat{a}^{\dagger}\hat{a}\delta t} \cdot e^{\gamma(Z)\hat{a}\otimes\hat{b}^{\dagger}} = \sum_{n,m,n',m',a} \frac{e^{-\frac{\kappa}{2}n\delta t}}{(m-n)!}\gamma(Z)^{m-n}\sqrt{\frac{m!}{n!}} \, W_{1,a}^{(p)n,m} W_{a,1}^{(pp)n',m'} |n\rangle \langle m| \otimes |n'\rangle \langle m'| \ , \tag{48}$$

with

$$\begin{cases} W_{1,a}^{(p)n,m} = \delta t_{m-n,a} \\ W_{a,1}^{(pp)n',m'} = \tilde{W}_{a,1}^{(pp)n',m'} = \delta t_{n'-m',a} \ . \end{cases} \tag{49}$$

At this point, obtaining the exact factorization of the effective Hamiltonian for the non-linear homodyne detection is straightforward. We start by defining $\kappa \langle\Psi(t)| (\hat{a}_{j}^{\dagger} + \hat{a}_{j}) |\Psi(t)\rangle \equiv f$, considering a single site, dropping the j subscript and writing

$$e^{(Z+f)\delta t\hat{a} - \frac{\kappa}{2}\delta t\hat{a}^{\dagger}\hat{a}}. \tag{50}$$

We see that the operator has the same form as 43 with $Z+f$ instead of f. Thus the factorized operator has the form:

$$e^{(Z+f)\delta t\hat{a} - \frac{\kappa}{2}\delta t\hat{a}^{\dagger}\hat{a}} = e^{-\frac{\kappa}{2}\hat{a}^{\dagger}\hat{a}\delta t} \cdot e^{(Z+f)\frac{1-e^{-\kappa\delta t/2}}{\kappa/2}\hat{a}} \ . \tag{51}$$

The MPO form of this operators is given by Eqs. (48) and (49) with $\gamma(Z) = (Z+f)\frac{1-e^{-\kappa\delta t/2}}{\kappa/2}$.

E   Physical Motivation for the System-Environment Model

Typical physical systems are immersed in a single global environment. For example, electrons in a real material are coupled to the atoms in the crystal structure, which vibrate collectively

through excited phonon modes. In this section, we sketch out the justification and physical approximations required for mapping a system coupled globally to an environment with a continuum of energy modes to the toy models that we have considered in this paper, where we have an effective (independent) mode coupled locally to each site of the lattice, with an effective correlation function that decays in time.

We begin with a system-environment interaction in the linear form,

$$\hat{H}_{\text{Int}} = \sum_{j,k} g_{j,k} \hat{L}_j \hat{a}_k^\dagger + g_{j,k}^* \hat{L}_j^\dagger \hat{a}_k, \tag{52}$$

where $\hat{L}_j$ act on system site j, $\hat{a}_k$ annihilates an excitation in mode k of the environment and the $g_{j,k}$ are some complex coefficients describing the coupling strength which in general are k dependent and may also be spatially inhomogeneous. We can then define *effective* environment modes,

$$\hat{\tilde{B}}_j = \sum_k g_{j,k}^* \hat{a}_k$$
$$\hat{\tilde{B}}_j^\dagger = \sum_k g_{j,k} \hat{a}_k^\dagger, \tag{53}$$

allowing us to write the interaction Hamiltonian as,

$$\hat{H}_{\text{Int}} = \sum_j \hat{L}_j \hat{\tilde{B}}_j^\dagger + \hat{L}_j^\dagger \hat{\tilde{B}}_j, \tag{54}$$

which is now of the form of the electron-phonon coupling in the Hubbard-Holstein model considered in the main text. However, we also need to consider the correlations between different effective environment modes, which in general will be non-zero and so not independent,

$$\begin{aligned}
\langle \hat{\tilde{B}}_{j'}(t') \hat{\tilde{B}}_j^\dagger(t) \rangle &= \sum_{k,k'} g_{j,k} g_{j',k'}^* \langle \hat{a}_{k'}(t') \hat{a}_k^\dagger(t) \rangle \\
&= \sum_{k,k'} g_{j,k} g_{j',k'}^* e^{-i\omega_k t + i\omega_{k'} t'} \langle \hat{a}_{k'} \hat{a}_k^\dagger \rangle \\
&= \sum_{k,k'} g_{j,k} g_{j',k'}^* e^{-i\omega_k t + i\omega_{k'} t'} \delta_{k,k'} \\
&= \sum_k g_{j,k} g_{j',k}^* e^{-i\omega(t-t')},
\end{aligned} \tag{55}$$

where in the second to last line, we have used the (zero-temperature) relation, $\langle \hat{a}_{k'} \hat{a}_k^\dagger \rangle = \delta_{k,k'}$, valid if the operators $\hat{a}_k^\dagger$ are the eigenmodes of the environment Hamiltonian, i.e. the environment is a collection of non-interacting bosons $\hat{H}_E = \sum_k \omega_k \hat{a}_k^\dagger \hat{a}_k$.

Next, we assume that the magnitudes of the coupling coefficients are homogeneous, but there can be a relative phase factor,

$$g_{j,k} = g_k e^{-ikja}, \tag{56}$$

where a is the spacing between lattice sites. We then arrive at the expression for the correlation functions,

$$\langle \tilde{B}_{j'}(t') \tilde{B}_j^\dagger(t) \rangle = \sum_k |g_k|^2 e^{-ika(j-j')} e^{-i\omega(t-t')}. \tag{57}$$

Following [167], we consider strong lattice confinement so that the eigenstates of the harmonic oscillator can approximate the localized basis for the fermions. Then, the coupling coefficients between such fermionic states and a continuous bosonic excitation in the environment described by a plane wave can be written as:

$$g_k^{\alpha,\beta} \propto \int \mathrm{d}z \, \Phi^{\alpha*}(z)\Phi^\beta(z)e^{-ikz}, \tag{58}$$

where $\Phi^\alpha(z)$ is the α-th eigenstate of the harmonic oscillator:

$$\Phi^\alpha(z) = \frac{1}{\sqrt{2^\alpha n!}}(\pi a^2)^{-1/4}e^{\frac{z^2}{2a_z}}H^\alpha\left(\frac{z}{a_z}\right), \tag{59}$$

where $a_z = \sqrt{1/m\omega_z}$ and H^α are the Hermite polynomials. Assuming only the ground states $\Phi^0(z)$ to be occupied, we can compute the coupling coefficients exactly:

$$g_k = ge^{-k^2a^2/2}, \tag{60}$$

where we have assumed a momentum-independent prefactor g. We now consider a linear dispersion relation $\omega = ck$ and insert the expression for g_k into Eq. (57). If $ka \gg 1$, then for $j \neq j'$, we get a large oscillating component in the sum, which leads to a vanishingly small correlation. This corresponds to the so-called large wave-vector limit, which is valid if the characteristic wavelength of excitations in the environment λ_{eff} is much smaller than the spacing between system lattice sites. Approximating the sum with an integral for $j = j'$ we obtain:

$$\langle \hat{\tilde{B}}_{j'}(t')\hat{\tilde{B}}_j^\dagger(t)\rangle = \sum_k |g_k|^2 e^{-i\omega(t-t')} \approx \int_0^\infty \mathrm{d}k \, |g_k|^2 e^{-ick(t-t')} \approx \int_0^\infty \mathrm{d}k \, g^2 e^{-k^2a^2 - ick(t-t')}$$
$$= \sqrt{\frac{\pi}{a^2}}g^2 e^{-c^2/4a^2(t-t')^2} \equiv \alpha(t-t'). \tag{61}$$

In Fig. 19 we approximate the correlation function Eq. (61) via the Laplace-Pade method [163]. It can be seen that already three complex exponentials suffice to reproduce the correlation function fairly well.

This then allows us to connect our work presented here to a wider variety of more realistic physical systems. An interesting future research direction would be analyzing what happens when this small wavelength limit is not satisfied, giving rise to strong correlations between the different environment modes.
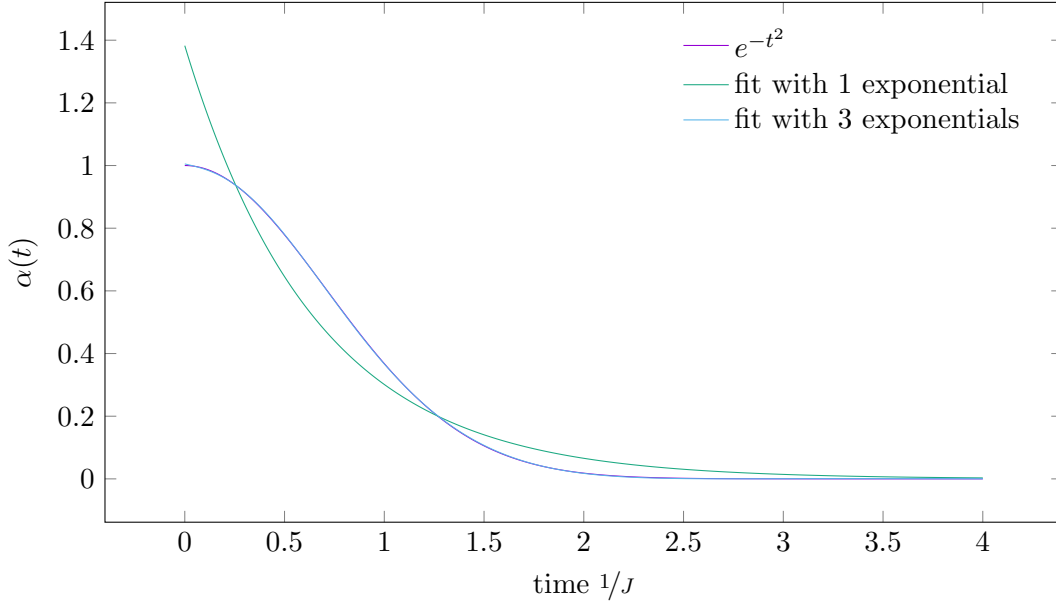
Figure 19: Bath correlation function Eq. (61) approximated with 1 and with 3 complex exponentials via the Laplace-Pade method for $c = g = a$.

F Failure of the Markovian Description of the Dissipative Hubbard-Holstein Model

The non-Markovian method outlined in Sec. 2.2 and the Markovian one for the enlarged physical system (electrons + phonons) discussed in Sec. 2.1 are numerically challenging. Thus, one could wonder whether a much simpler Markovian master equation for the electronic system only would suffice to describe the dynamics correctly. Such an equation was derived in [93] and reads:

$$\partial_t \hat{\rho} = -i[\hat{H}_{\mathrm{f}}, \hat{\rho}] + g^2 \big(\sum_{j=1}^{L} \hat{n}_j \hat{\rho} \hat{n}_j - \frac{1}{2} \{ (\hat{n}_j)^2, \hat{\rho} \} \big) \,, \tag{62}$$

where $\hat{H}_{\mathrm{f}}$ is the Hubbard Hamiltonian, g the electron-phonon coupling and $\hat{n}_j$ the number operator acting on the $j-$th fermionic site. Note that the Linblad equation 62 has been derived via the Markovian and the Born (i.e. weak coupling) approximation and is thus not expected to provide a valid description for large values of the electron-phonon coupling g. The exact-diagonalization comparison between the master equation for the enlarged system Eq. (2) and the master equation for the electronic system only Eq. (62), shows that the latter is not suited for describing the non-Markovian bath that arises when the phonons are traced out.
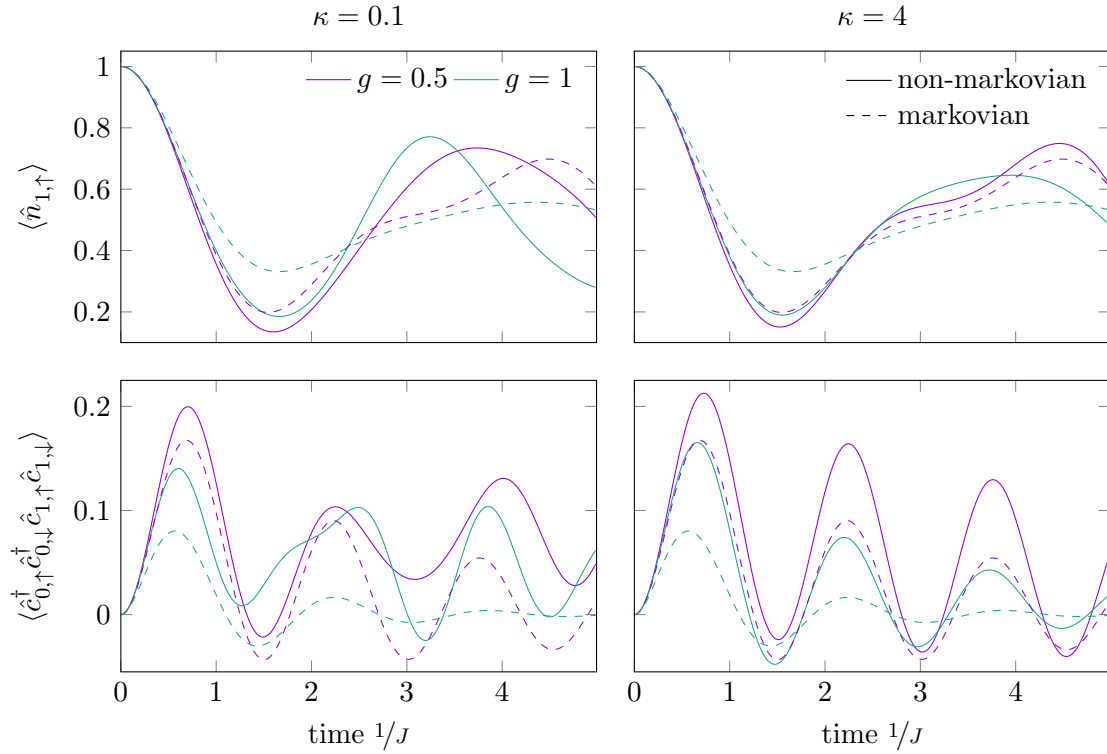
Figure 20: Comparison between a master equation for the "electron + phonon" system and a master equation for the electron system only. For all plots, the Hamiltonian parameters were chosen to be $U = J$ and $\omega = 2J$. The dissipation strength κ was fixed to $0.1\,J$ for the left plots and $4\,J$ for the right plots. The results obtained with the two methods strongly deviate from one another, showing that the electron dynamics of the systems considered here cannot be captured by the naive Lindblad master equation of the form 62.